

The Electromagnetically Isolated Global Signal Estimation Platform (EIGSEP)

Christian H. Bye,^{1,2*} David R. DeBoer,^{2,3} Matt Dexter,² Aaron Ewall-Wice,^{1,2} Adam Fahs,^{4,5} Pranav Karthik,^{1,2} Komal Kaur,^{1,2} Bahram Khalichi,^{1,2} Wei Liu,^{1,2} Raul A. Monsalve,^{5,6,7} Aaron R. Parsons,^{1,2} Reid Parsons,⁸ Richard R. Rodriguez,^{2,9} Richard J. Saeed,² Charlie G. Tolley,² Dominic Vazquez,^{2,9} and Dirk Wright^{1,2}

¹Department of Astronomy, University of California Berkeley, Berkeley, CA 94720, USA

²Radio Astronomy Laboratory, University of California Berkeley, Berkeley, CA 94720, USA

³Sub-department of Astrophysics, University of Oxford, Oxford, OX1-3RH, UK

⁴Department of Physics, University of California Berkeley, Berkeley, CA 94720, USA

⁵Space Sciences Laboratory, University of California Berkeley, Berkeley, CA 94720, USA

⁶School of Earth and Space Exploration, Arizona State University, Tempe, AZ 85287, USA

⁷Departamento de Ingeniería Eléctrica, Universidad Católica de la Santísima Concepción, Alonso de Ribera 2850, Concepción, Chile

⁸Earth and Geographic Sciences Department, Fitchburg State University, Fitchburg, MA 01420, USA

⁹Department of Physics & Astronomy, San Francisco State University, San Francisco, CA 94132, USA

Accepted XXX. Received YYY; in original form ZZZ

ABSTRACT

The Electromagnetically Isolated Global Signal Estimation Platform (EIGSEP) is a new instrument designed to measure the global 21-cm signal from Cosmic Dawn and the Epoch of Reionization, redshifted to frequencies below 250 MHz. To reduce spectral structure in the antenna beam associated with ground scattering, EIGSEP uses a shaped bowtie antenna suspended in a canyon 100 m above the ground. We describe the current system design of EIGSEP, including the rotating antenna platform, a transmitter antenna to characterise the beam of the bowtie antenna, and auxiliary ground antennas. We then discuss the EIGSEP calibration scheme, which incorporates traditional Dicke switching in the receiver, and novel approaches that include beam mapping, beam modulation, and interferometric cross-correlation. The instrument has been deployed near Marjum Pass, Utah, for testing and initial data collection. We discuss the site characteristics and present initial field measurements.

Key words: cosmology: dark ages, reionization, first stars – instrumentation – telescopes

1 INTRODUCTION

During the first billion years of cosmic time, the universe evolved from a relatively smooth expanse of hydrogen and helium to the complex, chemically enriched web we observe today (Furlanetto et al. 2006). This transformation was driven by the first generations of stars, galaxies, and black holes, whose radiation heated and ionized the intergalactic medium (IGM), while locally seeding stellar growth. Measurements of the cosmic microwave background (CMB; Planck Collaboration et al. 2020; Reichardt et al. 2021), quasar absorption spectra (Fan et al. 2006; Becker et al. 2015; Bosman et al. 2018, 2022; Eilers et al. 2018), deep galaxy observations (McLeod et al. 2015; Castellano et al. 2022; Naidu et al. 2022; Finkelstein et al. 2023; Meyer et al. 2025; Whitler et al. 2025), and Ly α emitter surveys (McQuinn et al. 2007; Ota et al. 2017; Tang et al. 2024; Umeda et al. 2025; Witstok et al. 2025) can constrain the patchy end of reionization. However, the early stages of our Cosmic Dawn ($50 \gtrsim z \gtrsim 12$), when the first stars and X-ray sources appeared, will remain beyond the reach of optical and infrared probes for the foreseeable future (Mason et al. 2015; Liu et al. 2016b).

The Cosmic Dawn is none the less accessible through observations

of the 21-cm hyperfine line of hydrogen (Madau et al. 1997; Shaver et al. 1999; Tozzi et al. 2000). Interferometers, including HERA (DeBoer et al. 2017; Berkhouit et al. 2024), LOFAR (van Harleem et al. 2013), the LWA (Eastwood et al. 2019), the MWA (Tingay et al. 2013; Wayth et al. 2018), NenuFAR (Munshi et al. 2024), PAPER (Parsons et al. 2010), and SKA-Low (Dewdney et al. 2009), aim to measure the spatial anisotropies of the 21-cm signal, to probe inhomogeneities in density, heating, and ionization of the IGM. Upper limits on the 21-cm power spectrum reported by these experiments are beginning to constrain models of reionization (Ghara et al. 2020, 2025; Mondal et al. 2020; Greig et al. 2021; Abdurashidova et al. 2022; HERA Collaboration et al. 2023).

Information in the global 21-cm signal, i.e. the monopole component, complements measurements of the spatial 21-cm fluctuations (Liu & Parsons 2016). At high redshifts, the global signal encodes information about the first luminous sources (Mirocha et al. 2017). Ly α photons from the first generations of stars couple the spin-temperature of hydrogen to the kinetic gas temperature, causing an absorption dip relative to the CMB at $z \approx 25$. Compact objects left over from the first stars emit X-rays that heat the gas, possibly driving it into emission at $z \approx 9$, before UV emission from widespread star formation ionizes the IGM and effectively eliminates the signal by $z \approx 5$ (Kulkarni et al. 2019; Bosman et al. 2022). The timing

* E-mail: chbye@berkeley.edu

and depth of the absorption feature are sensitive to the properties of the first galaxies, including their mass distribution, star formation efficiency, X-ray, Ly α , and UV production rates, and the escape fraction of ionizing radiation into the IGM (Barkana 2016; Liu & Shaw 2020). By independently constraining the optical depth of Thomson scattering in the CMB, the global 21-cm signal also helps to improve constraints on the sum of neutrino masses and on the amplitude of primordial fluctuations seeding large-scale structure (Fialkov & Loeb 2016; Liu et al. 2016a).

Some of the ongoing experiments targeting the global signal from the ground include EDGES (Monsalve et al. 2017b; Bowman et al. 2018; Cappallo et al. 2025), GINAN (McKay et al. 2025), LEDA (Price et al. 2018), MIST (Monsalve et al. 2024a), PRIZM (Philip et al. 2019), REACH (de Lera Acedo et al. 2022), RHINO (Bull et al. 2025), and SARAS (Jishnu Nambissan et al. 2021; Singh et al. 2022). Space-based missions are also proposed or underway, including CosmoCube (Artuc & de Lera Acedo 2025), DSL/Hongmeng (Chen et al. 2021), LuSEE-Night (Bale et al. 2023), and PRATUSH (Sathyaranayana Rao et al. 2023).

The EDGES experiment reported a detection of an unexpectedly large (~ 500 mK) 21-cm absorption trough in Bowman et al. (2018). If of cosmological origin, the measurement could imply new interactions between baryons, photons, and dark matter (Barkana 2018; Muñoz & Loeb 2018; Pospelov et al. 2018; Slatyer & Wu 2018; Sikivie 2019) or an excess radio background early in the Cosmic Dawn (Feng & Holder 2018) from previously undetected progenitors of super-massive black holes (Ewall-Wice et al. 2018, 2020), star-forming galaxies (Mirocha & Furlanetto 2019), or dark matter annihilation (Fraser et al. 2018; Yang 2018).

Alternatively, the absorption feature might be a systematic artifact of antenna interactions with the environment, cables, or ground planes (Hills et al. 2018; Bradley et al. 2019; Singh & Subrahmanyan 2019; Sims & Pober 2020). Such interactions complicate the removal of galactic foreground emission, which are more than four orders of magnitude brighter than the target signal (Di Matteo et al. 2002; Oh & Mack 2003) and pose the primary challenge for high-redshift 21-cm experiments. In principle, the spectral smoothness and spatial variability of the foregrounds allow them to be separated from the 21-cm global signal (Pritchard & Loeb 2010; Liu et al. 2013; Sathyaranayana Rao et al. 2017b). However, effects such as antenna beam chromaticity (Bernardi et al. 2015; Mozdzen et al. 2016), ionospheric scattering (Vedantham et al. 2014; Datta et al. 2016; Shen et al. 2021), and reflections off conductive elements (Spinelli et al. 2022; Agrawal et al. 2024; Monsalve et al. 2024b) introduce significant spectral structure into the measured antenna temperature, thus reducing the efficacy of foreground subtraction or filtering. Even low-level ($\sim 10^{-4}$) spectral structure in the antenna beam can result in features that mimic a cosmological signal (Switzer & Liu 2014).

In 2022, SARAS reported a non-detection of the EDGES feature at 95.3 per cent confidence (Singh et al. 2022). SARAS uses an antenna on a raft to set a minimum delay of reflections, corresponding to the light travel time to the bottom of the lake. This delay ensured that spectral ripples in SARAS data associated with reflections would have periods less than 1.5 MHz, enabling them to be distinguished from the 21-cm signal, which is expected to vary more slowly with frequency (Raghunathan et al. 2021; Singh et al. 2022). The tension between the EDGES and SARAS results emphasizes the need for experiments that are electromagnetically isolated from their environment at scales relevant for measuring the 21-cm signal.

Here, we introduce the Electromagnetically Isolated Global Signal Estimation Platform (EIGSEP), a new experiment that aims to measure the 21-cm global signal from the Cosmic Dawn and Epoch of

Reionization. Crucial to the EIGSEP design is the use of an antenna suspended in a canyon, about 100 m above the ground and from the nearest electric conductors. This distance suppresses ground coupling and confines spectral structure induced by reflections to long delays. Moreover, the electromagnetic isolation may enable accurate electromagnetic modelling of the antenna without detailed knowledge of the electrical properties of the ground. This isolation would greatly simplify the electromagnetic simulations of the antenna, and facilitate direct comparisons between simulations and measurements of the antenna beam pattern and impedance. EIGSEP also furnishes a rotating antenna platform, allowing us to change the projection of the antenna beam pattern on the sky during measurements. Rotations of the antenna produce different beam-weighted foregrounds that can be used to separate instrumental systematics from sky emission. Additionally, the rotating antenna enables the measurement of the beam pattern with a single stationary transmitter.

This paper is outlined as follows: We describe the design principles in section 2 followed by the system design in section 3 and the calibration scheme in section 4. We then give an overview of EIGSEP deployments to date, including discussion about the site and RFI, in section 5. Finally, we summarize the status of the experiment and future work in section 6.

2 DESIGN PRINCIPLES

The goal of the EIGSEP experiment is to measure the redshifted global 21-cm signal from the Cosmic Dawn and Epoch of Reionization. Distinguishing between the possible 21-cm models in the presence of foregrounds and instrumental systematics requires careful foreground removal to minimize signal loss and avoid the introduction of spurious features that mimic the real cosmological signal. Here, we outline the principles motivating the EIGSEP design, to enable this signal separation.

EIGSEP is taking a conservative approach to foreground removal, where spectral modes contaminated by instrument-weighted foregrounds are all explicitly removed from the data and not used to model the cosmological signal. Mathematically, we obtain the modes to remove from the data by constructing the spectral covariance matrix of the instrument-weighted foregrounds and diagonalize it to find the eigenmodes. The covariance matrix could either be derived from measurements or from simulations. In practice, projecting such foreground eigenmodes out of measured data can easily suppress systematics to the sub-mK level. The difficulty lies in ensuring that residuals still retain a measurable contribution from cosmological 21-cm emission. As noted above, the intrinsic foreground sky is spectrally smooth and may be described by low-order polynomials or maximally smooth functions (Pritchard & Loeb 2010; Sathyaranayana Rao et al. 2017b; Bevins et al. 2021). If an antenna or its environment can introduce spectral structure that spans the space of global 21-cm signal models, filtering off bright foreground modes leaves no cosmological signal behind. This issue might be alleviated by taking advantage of the spatial anisotropies of the foregrounds, to separate them from the monopole cosmological signal (Switzer & Liu 2014), or by observing with different instruments to separate systematics from sky emission (Saxena et al. 2023).

This approach leads to three specific design principles for EIGSEP:

- (i) The instrument spectral response can be modelled with a limited number of spectral modes, that have minimal overlap with the 21-cm signal modes.
- (ii) The instrument can be modified between or during measurements to produce different weightings of systematics.

(iii) The systematics of the instrument can be modelled and measured in the field.

In the rest of this section, we detail each principle and explain how they inform the EIGSEP design. We focus on the systematics associated with the chromatic antenna beam, which is typically the most challenging systematic to characterize for global signal experiments and is usually accounted for in numerical simulations (Mahesh et al. 2021; Cumner et al. 2022; Monsalve et al. 2024a). Frequency-dependent systematics introduced by the receiver are calibrated with lab measurements and in-situ Dicke switching, as outlined in section 4. We define in this section the spectral modes of the antenna as the eigenmodes of the spectral covariance matrix of an antenna beam averaged over pointings.

2.1 Minimizing Covariance with the 21-cm Signal

If the antenna beam and the foregrounds are described by N_{ant} and N_{fg} independent spectral modes respectively, then the beam-weighted foregrounds require of the order $N_{\text{modes}} \sim N_{\text{ant}}N_{\text{fg}}$ modes. The product N_{modes} is the number of degrees of freedom in the model used to fit and remove foregrounds from EIGSEP data. If this number is too large, the model becomes so flexible it can fit any feature in the data, including the cosmological signal. Furthermore, the task of characterizing the antenna beam pattern through both measurements and simulations – and comparing the two – is simplified by limiting the number of modes needed to describe the beam pattern. Several global signal experiments, including EDGES (Cappallo et al. 2025), MIST (Monsalve et al. 2024a), REACH (Cumner et al. 2022), and SARAS (Singh et al. 2022), use small antennas with simple geometries to ensure that the beam pattern varies smoothly with frequency. Using the terminology introduced here: their responses may be described by few eigenmodes. Another benefit of a simple geometry is that it streamlines electromagnetic simulations and reduces discrepancies between the simulated structure and the fabricated one. This simplicity improves the fidelity of the simulations and enables more reliable comparisons between simulations and measurements.

We therefore require a geometrically simple antenna for EIGSEP that can easily be manufactured and replicated. The frequency evolution of the antenna beam pattern must also be described by a limited number of modes. A useful heuristic for this number is the number of eigenmodes needed to explain the chromaticity of the antenna beam to about one part in 10^4 , roughly representing the dynamic range between the foregrounds and the expected cosmological signal.

Beyond the antenna geometry itself, the conductive environment around an antenna influences the beam chromaticity by creating multiple paths for a received wave to follow. The differential path lengths introduce a frequency-dependent interference ripple whose spectral scale is set by

$$\tau = \Delta\ell/c = 1/\Delta\nu, \quad (1)$$

where τ is signal delay, $\Delta\ell$ is the differential path length, c is the speed of light, and $\Delta\nu$ is the period of the resulting spectral ripple. Because global 21-cm signal models vary on scales of 10–100 MHz, equation 1 suggests that conductive structures within ~ 30 m of the antenna require careful scrutiny. Notably for global signal experiments, the presence of a ground plane below the antenna may potentially introduce spectral artifacts that are degenerate with global signal features, leading to spurious or hard-to-interpret results (Vedantham et al. 2014; Hills et al. 2018; Bradley et al. 2019; Singh & Subrahmanyan 2019; Sims & Pober 2020). On the other hand, experiments operating directly on the soil without a ground plane are finding that interpre-

tations of their results depend crucially on soil modelling (Spinelli et al. 2022; Monsalve et al. 2024b).

The nominal requirement for EIGSEP is electromagnetic isolation from structures within 100 m of the antenna. According to equation 1, this isolation will suppress spectral ripples with periods of $\Delta\nu \leq 1.5$ MHz, corresponding to $\tau \gtrsim 670$ ns. EIGSEP achieves this electromagnetic isolation by using an antenna suspended 100 m above the ground in the canyon. This concept is shown in Fig. 1. The only conductive structure within the 100 m air bubble is the antenna platform that holds the front-end electronics. This platform is in the near-field of the antenna and is included in electromagnetic simulations. We require that the metal platform and electronics be contained within 2 m of the antenna. The analogue signal from the antenna is transmitted over fibre-optic cables to the ground and the antenna is suspended with non-conducting Kevlar ropes.

To illustrate the effects of electromagnetic isolation, we simulate the contributions of the environment to the antenna reflection coefficient for the EIGSEP antenna at different heights above the canyon floor. The spectral shape of the reflection coefficient is dominated by reflections at the interface between the antenna and the receiver due to impedance mismatch. This shape is perturbed by spectral ripples from reflections off the canyon, in accordance with what we expect to see in sky measurements. In the simulations of the scattering, we use a digital elevation model of the canyon and assume a uniform conductivity and permittivity of the canyon soil. This is a simplified model, but the digital elevation model captures the geometry of the canyon that sets the spectral scales of the ripples. Specifically, we use the terrain model of the canyon to compute the distribution of delay-scales at which the reflected waves will appear at the antenna. The results are shown in Fig. 2, up to an undetermined scale factor in amplitude. It is seen clearly that increasing the suspension height moves reflections to longer delays. While this result is computed for a signal transmitted from the antenna, the same types of spectral ripples will be present in sky measurements.

2.2 Making Independent Measurements

Aside from spectral separation, another way to break degeneracies between beam-weighted foregrounds and the cosmological signal is to leverage the variability of the beam-weighted foregrounds. This is usually proposed in the context of using data from different LST bins, where the foregrounds change with the Earth rotation while the (monopole) cosmological signal stays constant (Switzer & Liu 2014; Tauscher et al. 2020; Anstey et al. 2023). A second possibility is to alter the instrument. For example, REACH plans to observe with two different antennas (de Lera Acedo et al. 2022; Saxena et al. 2023), and the EDGES (Cappallo et al. 2025), MIST (Monsalve et al. 2024a), and SARAS (Singh et al. 2022) experiments have been conducting observations with different instruments and at different sites.

Making independent measurements with different weighting of instrumental systematics is crucial to achieve a confident detection of the 21-cm signal. EIGSEP is a portable experiment that can observe from different sites, and we plan on making measurements with different antennas. Moreover, EIGSEP uses a rotating platform to change the instrumental systematics in a controlled way during observations. Two types of rotations are supported: azimuthal rotations of the antenna (similar to the LuSEE-Night turntable (Bale et al. 2023)) and axial rolls of the platform itself. A diagram illustrating the rotations is shown in Fig. 3. Measurements done at different antenna orientations change the beam weighting of the emission from the sky and the ground. In a manner similar to observations at different LST bins, the antenna rotations allow EIGSEP to project out shapes that

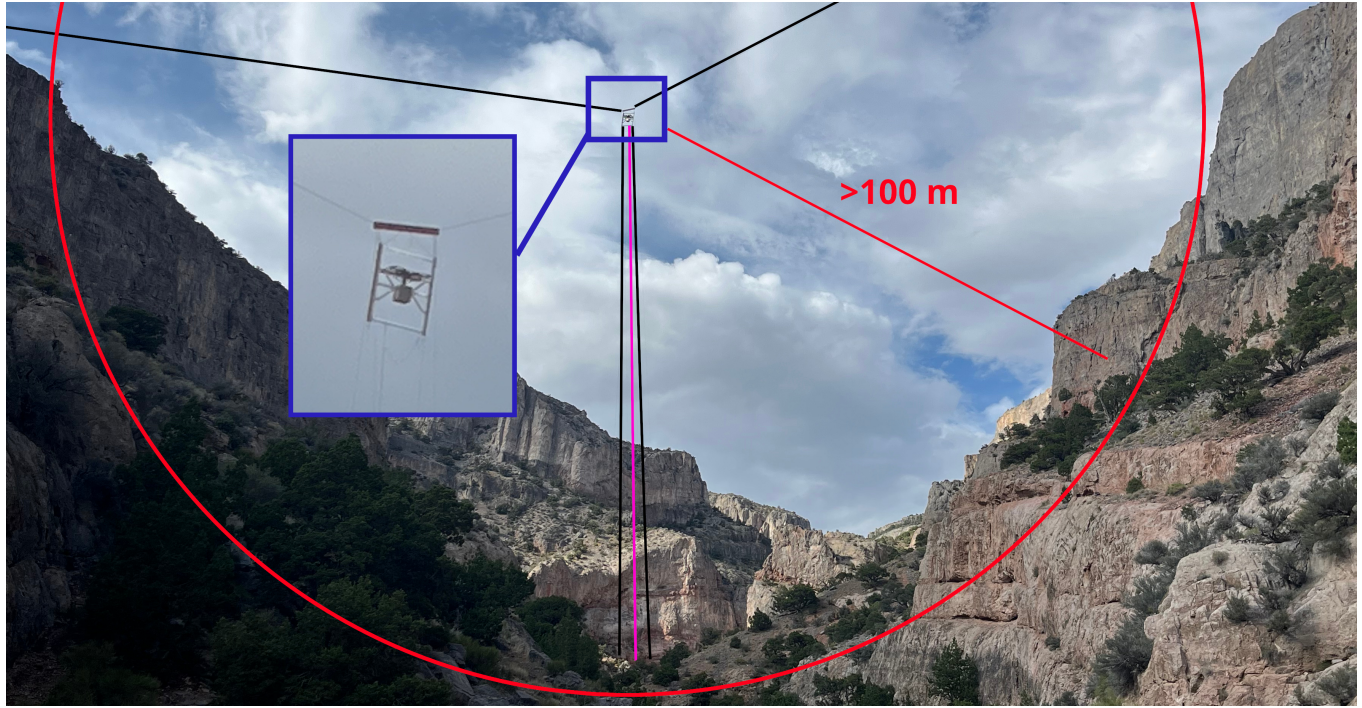


Figure 1. The EIGSEP concept: An antenna suspended in a canyon, with a 100 m zone free of electrical conductors. The inset shows a zoomed in view of the antenna. The conductor-free zone is shown in red, with the antenna in the middle of the canyon suspended from Kevlar ropes (black). The signal is transmitted to the backend electronics on the ground via non-conducting fibre-optic (pink).

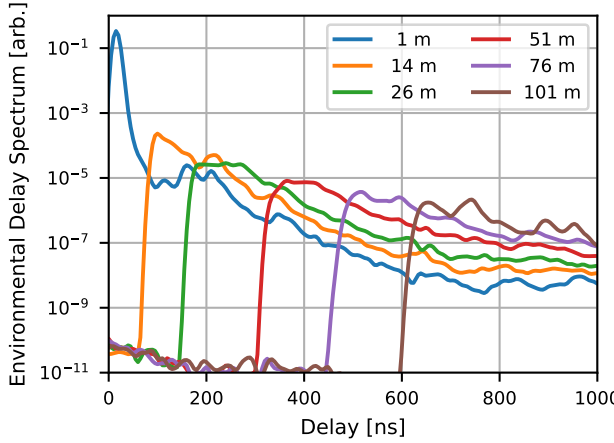


Figure 2. Delay–power spectra of simulated environmental scattering for the EIGSEP bowtie antenna suspended at different heights. The spectra show the environment-induced contribution to the antenna reflection coefficient. Environmental reflections appear at delays set by the two-way travel time of light between the antenna and the surrounding terrain, producing a height-dependent gap in delay space. As the height of the antenna increases, the gap in signal delay increases, due to increased light travel time to the environment. An antenna at 100 m suppresses reflections below 600 ns (brown). The curves are normalized by a common reference to highlight relative delay structure.

vary, as the global signal stays constant. In addition to the rotations, the platform height can be varied in the field to change the horizon profile or evaluate the coupling to the ground, which may impact signal recovery (Bassett et al. 2021; Pattison et al. 2024).

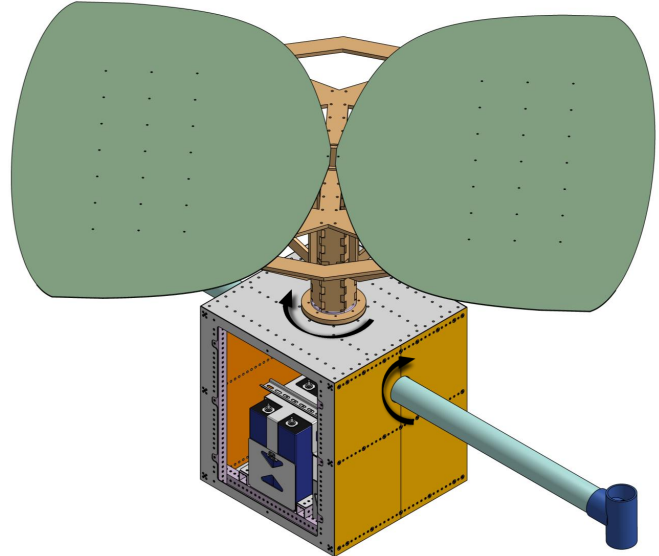


Figure 3. A CAD model of the EIGSEP antenna (green) on top of the antenna platform. The drawing does not include the copper plates that shield the sides of the box. The two black arrows represent the two types of rotations possible with EIGSEP.

2.3 Modelling and Measuring Systematics

The third design principle for EIGSEP is the ability to model systematics and measure them in the field, during observations. The relevant systematics associated with the antenna are the beam pattern and impedance. Both quantities are multiplicative and frequency-

Table 1. EIGSEP System Characteristics

Redshift Range	27.4–4.7
Bandwidth	50–250 MHz
Frequency Channels	1024
Frequency Resolution	244 kHz
Integration Time	1.07 s
Antennas	3
Correlations	11
Suspension Height	100 m
Fibre Length	305 m
Kevlar Length	305 m
Platform Weight	35 kg
Tether Tension	100 kg

dependent, and must therefore be known to a precision set by the dynamic range between foregrounds and signal, about one part in 10^4 (Cumner et al. 2024). While many experiments targeting the global 21-cm signal are measuring the impedance with a vector network analyzer (VNA), they often use commercial electromagnetic solvers to simulate the antenna beam pattern for calibration and chromatic corrections (Bowman et al. 2018; Anstey et al. 2021; Monsalve et al. 2024a). Validations of simulations are often indirect or focused on impedance measurements, due to challenges of measuring the antenna beam directly (Mahesh et al. 2021; Altamirano et al. 2025; Hendrickson et al. 2026).

For EIGSEP, we require that these quantities are measured in the field directly to increase our confidence in the calibration and validate simulations. The design of EIGSEP must be conducive to accurate electromagnetic simulations, and enable direct measurements in the field. The electromagnetic isolation of the EIGSEP antenna is again crucial, as realistic simulations of the antenna can be done without including models of the geometry or electrical properties of the soil below the antenna. The EIGSEP receiver has a VNA and a switch network to autonomously measure the antenna impedance in the field. In order to measure the antenna beam, EIGSEP uses a transmitter antenna placed on the ground directly below the suspended antenna. It is important that the transmitter be in the far-field of the suspended antenna. This specification is satisfied by the 100 m suspension height, a distance of more than 15 wavelengths at the lowest frequencies. To probe the direction-dependence of the beam, we rotate the antenna platform, thereby shifting the part of the beam sensitive to the transmitter.

3 SYSTEM DESIGN

The EIGSEP instrument is a three-element interferometer, with the main antenna suspended within the canyon and two antennas on the ground in the canyon. Front-end electronics, including a balun, low-noise amplifiers (LNAs) and RF filters are located directly next to each antenna. The analogue signals from all three antennas are digitized and correlated at a central node on the ground. In this section, we describe the instrument as built and deployed in the field. A summary of the system characteristics is shown in Table 1, and a block diagram is shown in Fig. 4.

3.1 Suspended Antenna

Following the requirements outlined in section 2, a shaped bowtie antenna has been developed as the main antenna for EIGSEP. The bowtie antenna has a simple geometry, an inherently wide bandwidth, and an approximately omnidirectional radiation pattern. In

advanced bowtie antenna designs, conformal analysis has led to modifications of the traditional triangular geometry into elliptical or half-elliptical structures. These shapes offer smoother current distribution and impedance closer to $50\ \Omega$ or $75\ \Omega$, traditionally used as characteristic impedance, thereby enhancing broadband performance. Since the flare angle of the antenna is inversely proportional to its input impedance, elliptical profiles help maintain a stable impedance across a wide frequency range.

Building on these principles, the proposed bowtie antenna design begins with a half-circular geometry. Exponential parametric equations are then applied to achieve a refined tapering profile, which is subsequently optimized for performance within the desired frequency band. In order to optimize the antenna, it is simulated with Ansys HFSS¹. Given a range of simulations, the antenna design is chosen to minimize the overlap of the spectral shapes of the beam pattern and reflection coefficient with models of the 21-cm signal. The design is optimized to operate within the 50–250 MHz frequency range. To enhance low-frequency performance, the antenna structure may be bent and loaded in future iterations.

Furthermore, analysis indicates that impedance matching can be significantly improved by incorporating a simple matching circuit that transforms the antenna's average impedance of approximately $75\ \Omega$ to $50\ \Omega$, which is the characteristic impedance of the rest of the system. EIGSEP therefore uses a custom balun board with a 3:2 transformer. We simulate the antenna in free space in HFSS, over a simple rectangular aluminium box representing the antenna platform. The model does not include any screw holes, slots, the PVC frame, or the wood support for the antenna. Additionally, we use a simplified model of the balun board in the simulation, with an ideal transformer. We present the simulated antenna reflection coefficient, Γ_{ant} , in Fig. 5. The result demonstrates a smooth reflection coefficient across the desired bandwidth and a good impedance match between the antenna and a $50\ \Omega$ reference impedance, with $|\Gamma_{\text{ant}}| < -10\ \text{dB}$ above 85 MHz. In practice, measurements of the reflection coefficient may deviate from Fig. 5 due to simplifications made in the simulations. Additionally, a measurement in the canyon will introduce spectral ripples at scales shown in Fig. 2. Future work will present calibrated measurements from the field.

Simulations of the antenna beam pattern are shown in Fig. 6, at 50 MHz, 150 MHz, and 250 MHz. The simulations show that the beam pattern is nearly omnidirectional at 50 MHz and becomes more directive with increasing frequency. In addition, the gain increases with frequency. The simulations show the smooth evolution of the beam pattern from 50 MHz to 150 MHz – the side lobes appear only above 150 MHz and can be seen in the simulation at 250 MHz. Due to the presence of the metallic box, the gain is slightly higher below the antenna (zenith angles greater than 90°) than above, most prominently seen in the simulation at 250 MHz.

3.2 Antenna Platform

The antenna is mounted on an aluminium box that serves as the antenna platform. The box has a square cross-section of side length 14 in (approximately 36 cm) and a height of 16 in (approximately 41 cm). Copper panels are attached to the outside of the box to provide additional shielding against RFI generated by electronics within the box. The dimensions of the box and the distance to the antenna were optimized in electromagnetic simulations to keep the reflection coefficient smooth across the frequency band of interest.

¹ <https://www.ansys.com/products/electronics/ansys-hfss>

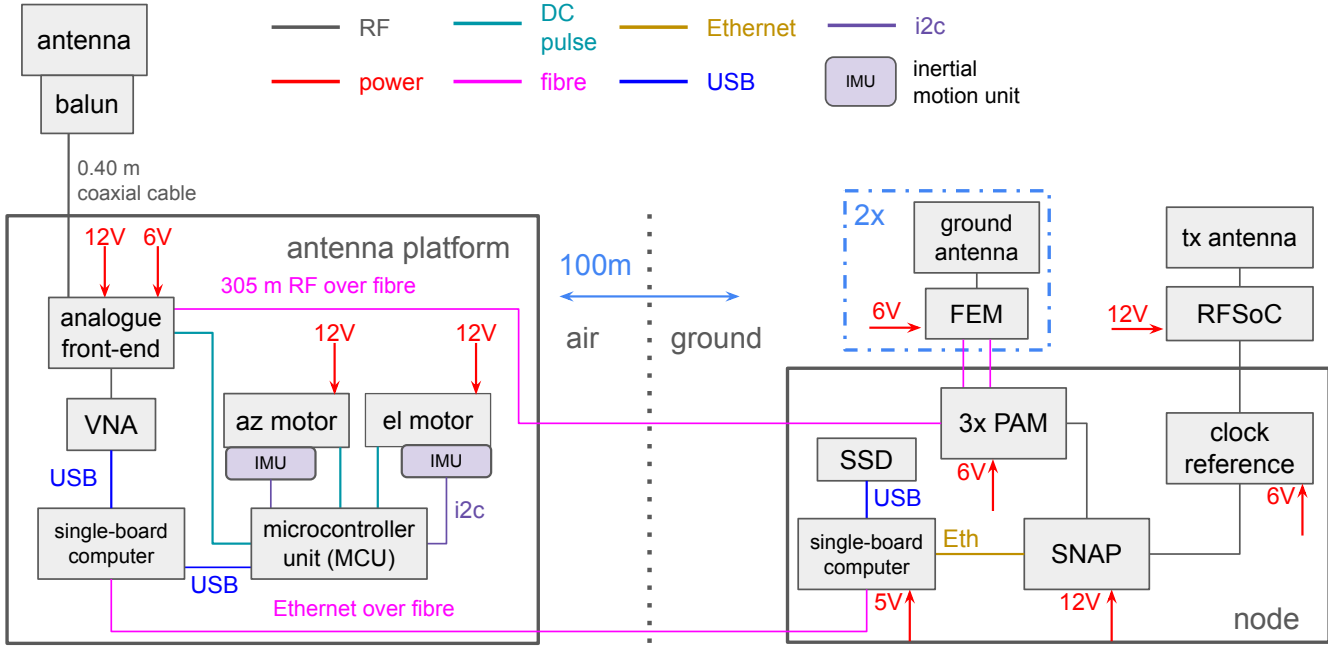


Figure 4. High-level block diagram of the EIGSEP instrument. The signal path for sky measurements goes from the antenna and ground antennas to the analogue front-end (the custom EIGSEP front-end for the suspended antenna, see Fig. 7, and the HERA FEM in the case of the ground antennas), through RF over fibre to the PAMs. Coaxial cables connect the PAM to the SNAP, where the signals are digitized and correlated. The SNAP uses Ethernet to communicate with the single-board computer, which saves the data to an external solid-state drive.

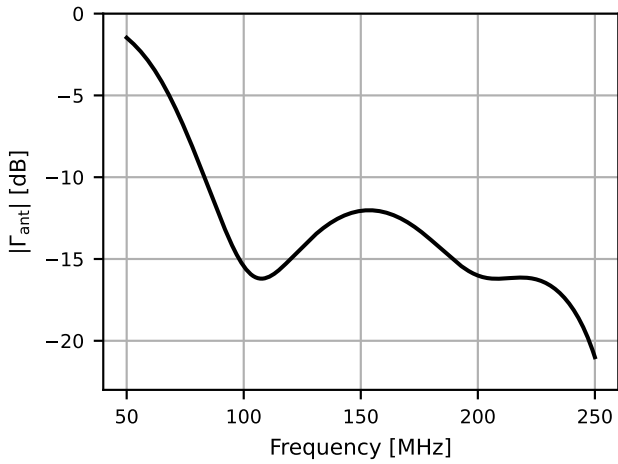


Figure 5. Magnitude of simulated antenna reflection coefficient for the bowtie antenna in free space as a function of frequency in dB.

The antenna is held 40 cm above the box and is mechanically attached to the box using a wooden structure. Wood was chosen because it is lightweight, strong, and non-conductive. During rotations of the antenna relative to the box, this structure rotates with the antenna.

As Fig. 1 shows, the box is suspended in the canyon using a frame big enough to support rotations of the antenna around the horizontal axis through the box. The frame is made of hollow Polyvinyl Chloride (PVC) pipes and suspended with 3/16 in Kevlar rope. Two lines of rope are strung across the canyon and tied to trees on top of each side. This double rope holds a pulley plate with two nylon pulleys.

Two suspension ropes and two safety lines go through the pulleys, tie to each side of the frame, and are anchored on the ground. Pulling on these ropes allows the antenna to be raised or lowered from the ground. The anchoring to the ground also helps prevent the antenna from moving significantly side to side.

The box can rotate around two axes, as described above and illustrated in Fig. 3. A stepper motor driving a slew drive is used for each rotation axis. This solution maintains the position of the box when the motors are not powered. By keeping track of the steps taken by each motor, and the starting position of the box, the orientation of the box can be derived. Each axis is also equipped with an inertial measurement unit (IMU), giving independent verification of the box orientation.

In addition to the motors, the box houses the analogue front-end electronics for the signal chain, and digital electronics controlling the box. The analogue chain is powered by 6 V batteries. 12 V batteries are used to power the motors and the digital electronics; separate 12 V batteries power the RF switches and noise diode (see Section 3.3). Using separate batteries increases the isolation between the analogue signal chain and noisy digital electronics.

3.3 Front-End Electronics

A prototype of the EIGSEP signal chain is developed and used for observations. The suspended bowtie antenna has a custom-made front-end specifically developed for EIGSEP. This front-end is described in this section and shown schematically in Fig. 7. The two ground antennas use Front-End Modules (FEMs) developed for the Hydrogen Epoch of Reionization Array (HERA; DeBoer et al. 2017; Berkhouwt et al. 2024). Details about the ground antennas and the FEMs are provided in Section 3.5.

After the balun, which is placed at the feed of the bowtie an-

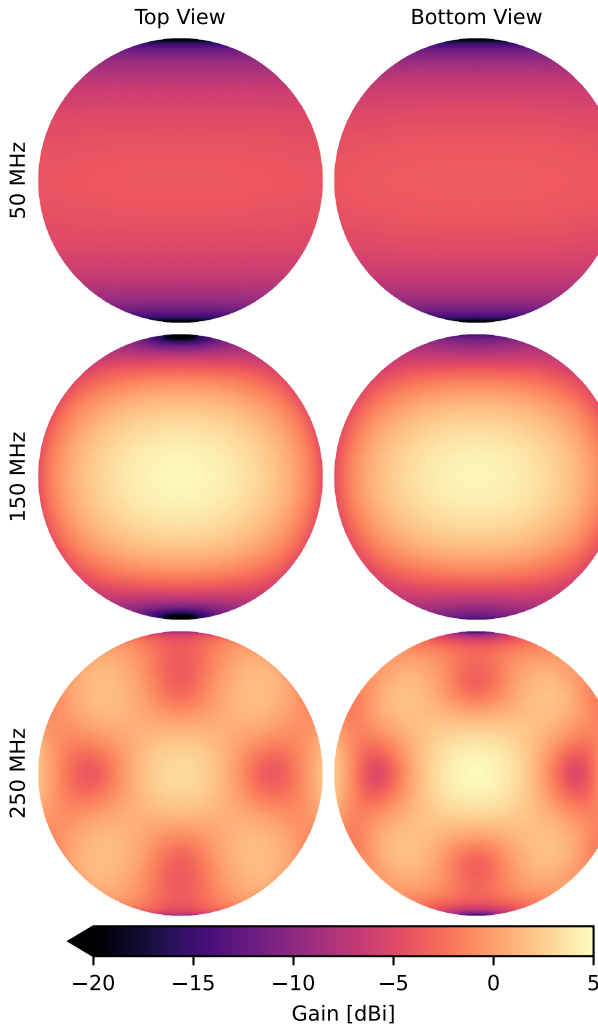


Figure 6. Simulated realized gain in dBi of the bowtie antenna at 50 MHz (top row), 150 MHz (middle row), and 250 MHz (bottom row). The columns show the beam projected from above the antenna (top view, left column) and below the antenna (bottom view, right column). The low-end of the colour scale is clipped at -20 dBi for visual clarity; the gain at 50 MHz has an actual minimum of ≈ -35 dBi.

tenna, a 40 cm coaxial SMA cable leads through the central column of the wood platform and connects to the receiver in the box. The first component inside the box is the RF switch network. There are seven electromechanical switches in the network, of the type Teledyne CCR-33S. They are fail-safe, single pole, double throw (SPDT) switches and the network follows the design used by MIST (see fig. 17 in Monsalve et al. 2024a). According to the datasheet, the switches provide 70 dB of isolation and have a maximum insertion loss of 0.2 dB. They require continuous 200 mA to be switched to the high-power state and remain in the low-power state if no power is supplied.

The main signal path through the switches connects the antenna to the receiver for sky observations. The other switch positions are used for calibration, including reflection coefficient measurements with a VNA and noise source measurements to set the temperature scale. A relay switch is used to turn the noise diode on and off. The

calibration subsystems are described in section 4. Here we focus on the amplification chain used for sky observations.

EIGSEP’s amplification chain uses a Mini-Circuits ZX60-P103LN+ as the first LNA. At 50 MHz, this LNA has a gain of 25.3 dB and noise figure of 1.2 dB. The ambient temperature of the LNA is monitored with a thermistor. As shown in the system diagram in Fig. 7, the LNA is followed by a 6 dB attenuator, filters providing a bandpass of 50–250 MHz, a second attenuator, and an RF-over-fibre (RFoF) module. The RFoF module is a custom-printed circuit board derived from a design developed for the DSA-2000 telescope (Hallinan et al. 2019). This module features two onboard amplifiers and a laser diode that modulates the RF signal to optical wavelengths for transmission over fibre-optic cable. The total gain of the onboard amplifiers is ≈ 40 dB. We made small modifications to the original board, including changing the trace width for impedance match and changing the onboard filters to match the EIGSEP frequency range. We also added a 6 dB external attenuator between the second amplifier and the diode to reduce reflections. Both the original design and the modified version of the RFoF board are open sourced under the CERN OHL S-V2 licence. They are available at <https://gitlab.com/dsa-2000/asp/rfot/ftx> and <https://github.com/liuweiseu/rfot/ftx/tree/cefad78>, respectively. The amplification chain as implemented in 2025 is illustrated in Fig. 8.

A single-mode fibre-optic cable connects the front-end in the box to the post-amplification module on the ground. The cable is 1000 ft (305 m) long and is not conductive. The long cable ensures that any potential cable reflections have delays of at least 3000 ns – long enough that they can be filtered from the measured spectra without signal loss (Ewall-Wice et al. 2016; Kern et al. 2019).

3.4 Digital Electronics

The LattePanda Mu² single-board computer is used in the box to control the motors, the switches, and the VNA. It has an x86 processor that allows it to run the VNA software. The computer is connected to the microcontroller unit (MCU), which consists of six Raspberry Pi Pico microcontrollers that interface with the switches, the motors, the IMUs, and the temperature sensors. The computer connects to a separate single-board computer on the ground through Ethernet over a digital fibre-optic link. The computer, MCU, and VNA form a unit placed inside a separate metal box within the antenna platform box to minimize self-RFI.

3.5 Ground Antennas

Two Vivaldi feeds of the type developed for HERA Phase II are used as ground antennas. Each Vivaldi feed features two orthogonal blades, enabling dual-polarization measurements. The antenna is optimized over 50–250 MHz, where it is impedance matched to the HERA FEM with a reflection coefficient of about -10 dB. Like the custom EIGSEP front-end, the HERA FEM has an RFoF module, and connects to fibre-optic cables at the output. The same type of fibre-optic cables are used for the ground antennas as for the suspended antenna. The Vivaldi feed and HERA FEM are described in detail in Fagnoni et al. (2021) and Berkhout et al. (2024). While HERA uses the Vivaldi feeds to illuminate a 14-m dish, EIGSEP uses the feeds in isolation without a dish. This choice keeps the instrument portable and reduces cost (Cumner et al. 2022).

² <https://www.lattepanda.com/lattepanda-mu>

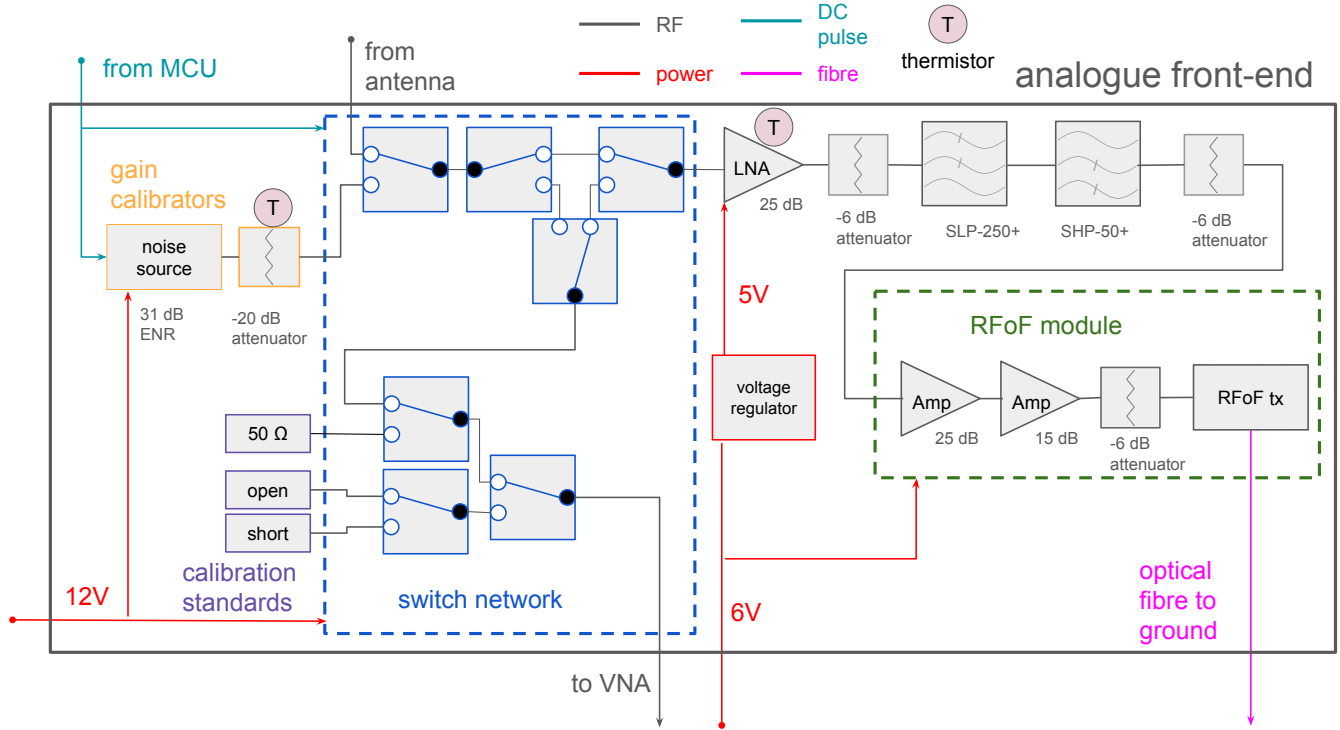


Figure 7. Block diagram of the front-end connected to the suspended antenna.

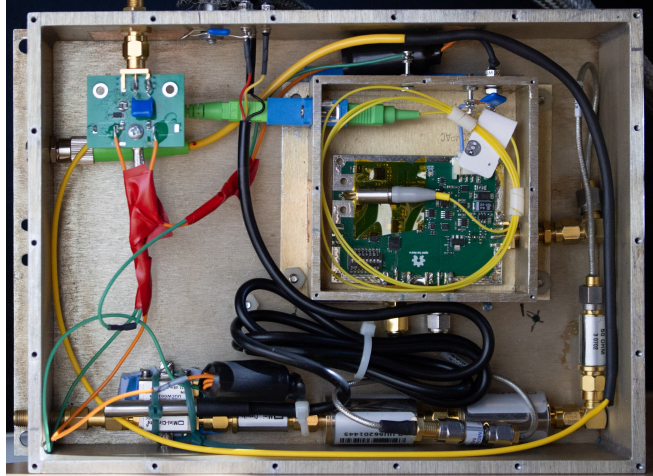


Figure 8. The amplification chain for the bowtie antenna. The RF signal input is in the bottom left corner. The signal goes counterclockwise through the amplifiers and filters on the bottom and right-hand side of the picture, through the RFoF module inside the inner box, and out through the optical output on the top left.

The FEMs feature an internal load and active noise source, but there is no autonomous switching between sky measurements and these devices in the current EIGSEP design. Only the receiver used for the suspended antenna will be absolutely calibrated. In future versions of the system, the same level of calibration may be attempted for the ground antennas.

3.6 Post-Amplifiers and Correlator

On the ground, the fibre-optic cables from each of the three antennas connect to a HERA post-amplifier module (PAM). The HERA PAM was co-designed with the HERA FEM and is also detailed in Fagnoni et al. (2021) and Berkhouwt et al. (2024). In each PAM, the optical signal is converted back to radio frequencies and amplified to levels appropriate for digitization. The PAMs are housed in an RF-shielded and watertight enclosure.

The final stage of the signal chain is the Smart Networked ADC Processor (SNAP). The SNAP is an FPGA-based digital signal processing module co-designed by HERA and the Collaboration for Astronomy Signal Processing and Electronics Research (CASPER; Hickish et al. 2016; DeBoer et al. 2017). It digitizes five inputs, one from the suspended antenna and two from each ground antenna, with 8-bit Hittite HMCAD1511 ADCs at 500 Msps. The SNAP channelizes the five inputs with a 2048-point Polyphase Filter Bank. Integrated correlations are computed every 1.07 seconds and output via 1 Gb Ethernet to a Raspberry Pi. The current version of the correlator computes eleven correlations: five autocorrelations and six cross-correlations. The cross-correlations consist of the four products formed between the single-polarization suspended antenna and the two dual-polarization ground antennas, in addition to the two co-polarized products (N–N and E–E) between the ground antennas.

A low-power single-board computer (Raspberry Pi) writes correlation data to USB storage, configures the SNAP, and records sensor data. The Raspberry Pi is housed inside a metal box. The total data volume is approximately 5 GB for 24 hours of observation. Fig. 9 shows the FEM, PAM, SNAP, and Raspberry Pi.



Figure 9. Components of the EIGSEP receiver as deployed in the field. *From left to right:* The FEM receives the analogue signal at each ground antenna, amplifies it, and transmits it with RFoF to the node. Each FEM connects to a PAM via optical fibre, in the same way the custom front-end at the suspended antenna connect to a PAM. The three PAMs are housed together. Analogue signals from the three antennas are digitized in the SNAP and correlated. On top of the SNAP is the enclosed Raspberry Pi, which programs the SNAP and saves data to disk. Each component is placed inside connectorized RF-tight enclosures.

4 CALIBRATION METHODOLOGY

Measurements of the global 21-cm signal require exquisite calibration due to the large dynamic range between the foregrounds and the signal. An important part of this requirement is to establish an absolute calibration scale, which converts measured voltages to sky temperature, taking all gains, losses, and reflections in the signal path into account. In general, these are frequency-dependent quantities, meaning that imprecise calibration – even at a low level – may artificially introduce spectral shapes that resemble the global 21-cm signal.

Instrumental systematics come in three distinct flavours:

- (i) Additive bias such as amplifier noise and impedance mismatch, which adds frequency-dependent signal power.
- (ii) Direction-independent multiplicative bias from, for instance, amplifiers, filters, and cable reflections, or due to impedance mismatch, which modulate foreground-dominated signals with a multiplicative bandpass.
- (iii) Direction-dependent multiplicative bias from the antenna beam and surrounding environment, which imprints incoming radiation with a multiplicative distortion as a function of direction.

Due to the stringent calibration requirements, a key aspect of the EIGSEP approach is using independent measurements to calibrate the same features. Independent measurements reduce the reliance on any one method, and the measurements can be used to validate each other. Below, we describe the mathematical model of our measurements and outline the methodology used to calibrate the instrumental systematics.

4.1 Model of Measurement

The suspended antenna measures a frequency-dependent temperature $T_{\text{ant}}(\nu)$ that can be written as

$$T_{\text{ant}}(\nu) = \int_0^{2\pi} \int_0^\pi A(\nu, \theta, \phi) T_{\text{emit}}(\nu, \theta, \phi) \sin \theta d\theta d\phi, \quad (2)$$

where A is the normalized antenna beam pattern and T_{emit} is the temperature associated with any emission from the sky or from the

ground. Both quantities are functions of frequency ν and the angles θ and ϕ on the sky. In equation 2, the antenna beam pattern A is normalized over the sphere such that

$$\int_0^{2\pi} \int_0^\pi A(\nu, \theta, \phi) \sin \theta d\theta d\phi = 1. \quad (3)$$

In this formalism, A does not include losses associated with the finite conductivity of the antenna or impedance mismatches. Instead, we incorporate these into the receiver gain g_{rx} , defined below.

Aside from RFI, which we assume is already removed in this model, T_{emit} is primarily a sum of sky emission T_{sky} and ground emission T_{gnd} . EIGSEP aims to measure T_{sky} , but, as seen in Fig. 6, the antenna is very sensitive to ground radiation. This radiation includes thermal radiation and reflected sky emission, delayed by the light travel time from the ground to the antenna. Due to the electromagnetic isolation of the EIGSEP antenna, we anticipate that most of the reflected sky emission can be filtered in delay space, and the remaining reflected emission is heavily attenuated due to the long distance. Thus, we assume that the residual T_{gnd} is dominated by thermal emission associated with the physical temperature of the environment.

For brevity, we drop the explicit dependencies on ν , θ , and ϕ in the notation. We may rewrite equation 2 by separating T_{emit} into T_{sky} and T_{gnd} . We denote the part of the sky that is not blocked by the canyon walls by Ω_{above} , and the ground and the canyon walls by Ω_{below} . We get

$$T_{\text{ant}} = \int_{\Omega_{\text{above}}} AT_{\text{sky}} \sin \theta d\theta d\phi + \int_{\Omega_{\text{below}}} AT_{\text{gnd}} \sin \theta d\theta d\phi. \quad (4)$$

The power P_{ant} received from the suspended antenna, measured as the autocorrelation spectrum, is related to the antenna temperature T_{ant} and the gain (g_{rx}) and the temperature (T_{rx}) of the receiver by

$$P_{\text{ant}}(\nu) = g_{\text{rx}}(\nu) (T_{\text{ant}}(\nu) + T_{\text{rx}}(\nu)). \quad (5)$$

For every measurement of P_{ant} , the EIGSEP calibration first involves solving for T_{ant} in equation 5. We then require accurate models and measurements of the antenna beam A and of the horizon profile to estimate T_{sky} from equation 4. A direct inversion of equation

⁴ may not be necessary to extract the 21-cm global signal, but we likely need accurate understanding of the spectral modes of A and T_{sky} . The details of the signal extraction and estimates of the constraining power of EIGSEP are left for future work. In the remainder of this section, we focus on the calibration needed to obtain T_{ant} and A .

4.2 Receiver Calibration

To measure system gain and characterise the bandpass, EIGSEP is working to implement a version of the receiver calibration formalism pioneered by EDGES. The method is detailed in [Rogers & Bowman \(2012\)](#) and [Monsalve et al. \(2017a\)](#); here, we give a summary of the implementation for EIGSEP.

We need to determine the receiver gain and temperature to invert equation 5 and solve for T_{ant} . In the field, the EIGSEP receiver switches between measuring the antenna and the internal noise source. When the noise source is off, the measured noise temperature is the physical temperature of the -20 dB attenuator. The off condition represents the ambient load, and we monitor its physical temperature with a thermistor. When the noise source is on, the injected noise temperature increases from that of the ambient load by a factor given by the excess noise ratio (ENR) of the noise source. These two calibration measurements can be combined to obtain a first-order estimate of the antenna temperature (equation 1 in [Monsalve et al. 2017a](#)). This estimate does not account for reflections at the interface between the antenna and the receiver due to impedance mismatch or that the noise is injected at a different switch position from the receiver input. The calibration of these effects requires measuring the reflection coefficients of the antenna and the receiver, and the receiver noise wave parameters ([Meys 1978](#)). The noise wave parameters are five frequency-dependent parameters that represent noise from the LNA reflected at the interface between the antenna and the receiver, and corrections to the assumed injected noise temperature of the ambient load and noise source. We will determine these by measuring four external calibration standards in the laboratory, following the procedure in [Monsalve et al. \(2017a\)](#).

In our calibration formalism, we have implicitly absorbed into g_{rx} and T_{rx} the reflection coefficients of the antenna and receiver, the antenna radiation efficiency, and the loss from the balun. While the reflection coefficients are measured in the field, we rely on electromagnetic simulations of the antenna to determine the radiation efficiency. The efficiency of the balun will be determined through a combination of simulations and laboratory characterisation of the S-parameters, following [Monsalve et al. \(2024a\)](#).

4.3 Reflection Coefficient Measurements

EIGSEP employs a Copper Mountain Technologies R60 1-port VNA for measurements of the antenna and receiver reflection coefficients. These coefficients are periodically measured in situ. The VNA is calibrated following the procedure used by EDGES and MIST ([Monsalve et al. 2017a, 2024a; Bowman et al. 2018](#)). Immediately before each measurement of the antenna reflection coefficient, the VNA is used to measure internal open, short, and load (OSL) calibration standards. This set of measurements provides a first-order calibration with the reference plane internal to the receiver. The reflection coefficient of the receiver is measured with a lower power level, to avoid saturation of the LNA. We repeat the OSL calibration of the VNA at this power level prior to the receiver reflection coefficient measurement. To shift the reference plane of the measurements to the receiver input, the S-parameters associated with cables and switches inside the receiver

are de-embedded. These S-parameters are measured in the laboratory using the S911T calibration standards from Copper Mountain Technologies.

4.4 Interferometric Measurements

In the SNAP, EIGSEP’s auxiliary ground antennas are cross-correlated with the suspended antenna. The ground antennas are oriented north-south in the canyon and can be separated by up to 300 m from each other thanks to the length of the fibre-optic cables. The antennas are portable and can be moved if another baseline is desired.

The cross-correlation measurements can be useful for observing bright celestial sources and characterising system gain. In particular, Cygnus A passes $\sim 1.5^\circ$ from the zenith at the site and has a well-characterised and absolutely calibrated spectrum ([Baars et al. 1977; Perley & Butler 2017](#)), making it a good external calibration reference for EIGSEP.

Measurements from ground antennas are also used to identify RFI and evaluate terrain coupling.

4.5 Antenna Beam Mapping

To calibrate the direction-dependent and frequency-dependent antenna beam, EIGSEP will use a combination of numerical electromagnetic simulations and field measurements. Simulations are done in HFSS and produce both predictions for the antenna reflection coefficient and antenna beam pattern.

EIGSEP aims to measure the beam pattern of the suspended antenna using a transmitting antenna placed on the ground directly below. The transmitting antenna used is an electrically short dipole antenna; the first implementation was with an RTL-SDR Blog Dipole Antenna³, of total length 46 cm. The antenna transmits a sequence of Dirac delta functions on every 16th channel (≈ 3.9 MHz) across the frequency band, generated by a digital-to-analogue converter (DAC) on a Xilinx Radio Frequency System-on-Chip (RFSoC) 2x2⁴. The clock of the RFSoC transmitter board is synchronised with the clock of the SNAP correlator, ensuring that the transmitted signal is exactly a Dirac comb with no spectral leakage. A picture of the transmitter is shown in Fig. 10.

The transmitter antenna is continuously transmitting during the observations. With no spectral leakage of the Dirac comb, the transmitted power is confined to 64 designated frequency channels. In the other channels, equation 4 still applies as the model for our measurements without contamination of the transmitted signal. We set the transmit power level P_{tx} high enough to dominate all other emission in the transmitter frequency channels, where the model for our measurement becomes (instead of equations 4 and 5)

$$P_{\text{ant}}(\nu_{\text{tx}}) \propto A(\nu_{\text{tx}}, \theta_{\text{tx}}, \phi_{\text{tx}}) P_{\text{tx}}, \quad (6)$$

where ν_{tx} denotes the transmitter frequency channels and the transmitter is at the position $(\theta_{\text{tx}}, \phi_{\text{tx}})$ defined in the local coordinate system of the antenna. Here, we treat the transmitter as a point source. The proportionality constant depends on the properties of the transmitter antenna – such as radiation efficiency, gain, and reflection coefficient – while the systematics of the suspended receiving antenna are calibrated (section 4.2). Future work will explore calibration schemes for the transmitting antenna. Since we know exactly

³ <https://www rtl-sdr.com/>

⁴ <https://xilinx.github.io/RFSoC2x2-PYNQ/>

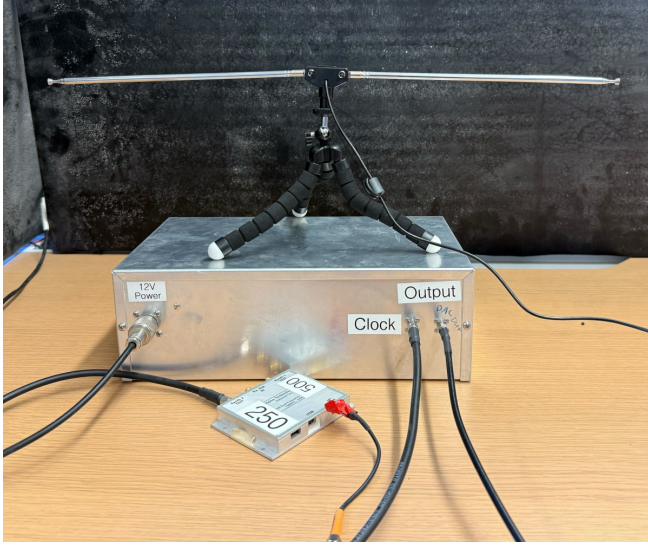


Figure 10. The short dipole antenna used to transmit into the bowtie antenna. The antenna is connected to the RFSoC board, placed inside the metal box underneath the antenna, which generates the transmitted Dirac comb. The clock is seen in front of the RFSoC box. During field measurements, the metal box is separated from the antenna to minimize its impact on the antenna performance.

what signal we are generating in the DAC, we can measure it with a spectrometer at the output to calibrate the analogue signal chain. The main challenge is characterising the frequency-dependent systematics of the transmitter antenna itself. We will explore various approaches to minimise these systematics, such as using electrically short antennas that can be described analytically (e.g. Balanis 1982) or using multiple transmitter antennas with different systematics. In addition, the transmitter antenna could be suspended or equipped with a ground plane to reduce ground coupling. By rotating the suspended antenna, the position $(\theta_{\text{tx}}, \phi_{\text{tx}})$ of the transmitter changes in the topocentric coordinates of the antenna. Thus, we probe a different spatial direction of A for each orientation. By rotating both axes, we can trace out the full spatial dependence of the antenna beam.

A secondary benefit of transmitting during observation is to monitor the stability of the receiver gain. It could also provide an independent measurement of the receiver gain if we achieve absolute calibration of the transmitter.

4.6 Antenna Beam Modulation

By rotating the antenna platform, EIGSEP can change the projection of the antenna beam pattern on the sky and terrain during observations. The canyon in which the antenna is suspended has a horizon profile that varies significantly with azimuth angle, as shown in Fig. 11. The profile represents the integration domain Ω_{below} in equation 4. As the antenna rotates, the weighting of the emission coming from the sky and from the ground changes. Rotations at time-scales much faster than that of the Earth rotation produce changes in A in equation 4, while T_{sky} and T_{gnd} remain effectively constant. These independent modulations will help us separate the effects of the antenna beam from the intrinsic sky emission.

Furthermore, we aim to measure and project out spatial foreground modes by rotating the antenna. When the antenna rotates, it will be sensitive to different parts of the sky. Because the 21-cm monopole

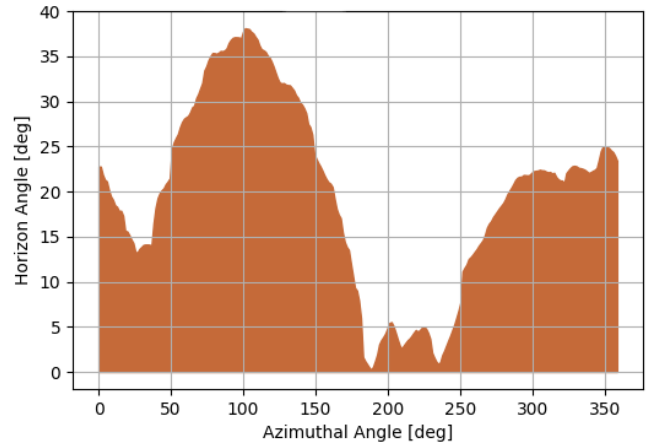


Figure 11. Horizon profile at the antenna site as a function of azimuthal angle. The brown area represents the canyon terrain (Ω_{below}) while the white area is the view of the sky (Ω_{above}).

is constant across the sky, we can use this modulation to remove foregrounds. We note that some change in the spectrum is due to different weighting of the sky and the ground (equation 4), but this effect can be estimated with models and measurements of the antenna beam pattern A and of the ground temperature T_{gnd} , which we assume to be close to a blackbody after filtering reflections. This technique is similar to fitting spectra from different LST bins to improve foreground modelling and subtraction (Liu et al. 2013; Tauscher et al. 2020; Anstey et al. 2023), but with the added benefit that the direction and timing of the rotation are not fixed to the Earth rotation. For EIGSEP, we aim to use both to improve constraints.

4.7 Sky Simulations

With an increasing focus on accurate modelling of diffuse synchrotron and point-source emission at low frequencies (de Oliveira-Costa et al. 2008; Sathyaranayana Rao et al. 2017a; Zheng et al. 2017), comparing data to direct sky simulations is becoming a viable approach for validating calibrated data. EIGSEP uses the CROISSANT simulation package⁵ to generate synthetic datasets given models of the foreground and antenna beam. While current models do not have the accuracy to calibrate the instrument alone, they none the less present an additional cross-check on calibration that can be used for verification. In particular, given a good enough beam model from measurements (section 4.5), it is possible to use EIGSEP data to solve for the sky emission and compare with sky models.

5 DEPLOYMENTS

Early versions of the EIGSEP instrument were deployed in the field in 2023 and 2024, primarily to characterise the instrument and the site while the instrument was under development. The version of the EIGSEP instrument described in this work was deployed in July 2025. The deployment site is Marjum Pass, Utah (39.2477° N, 113.4033° W) in the western United States. The site is remote, with steep topographical relief far from radio transmitters. It was selected from among a dozen candidate sites on the basis of broadband surveys

⁵ <https://github.com/christianhbye/croissant>

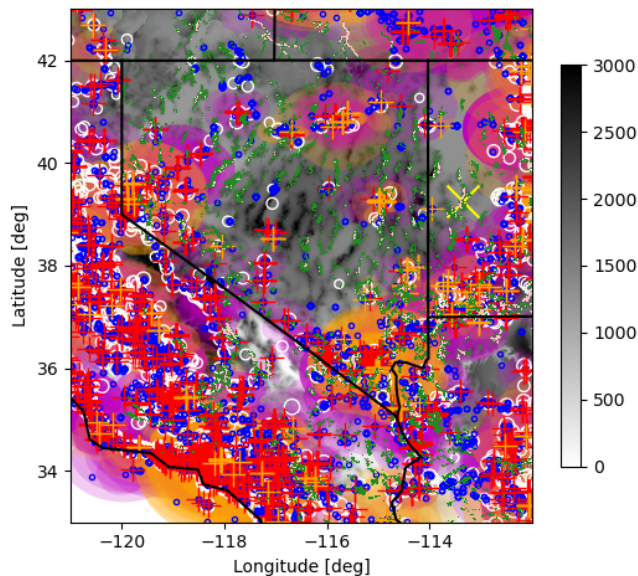


Figure 12. Digital Elevation Map (greyscale, m) of the western US with areas on public land with topographic features > 100 m on either side in green, and the deepest > 95 percentile in pink. FCC-registered FM and TV stations are shown in magenta and orange, respectively, with crosses at the transmitter and shading inside modelled 60 dBu contours. Blue circles indicate registered, but possibly inactive, FM and TV antennas. White circles indicate city centres. The yellow X marks the selected EIGSEP site.

showing very low levels of RFI. The deployments have established the site as a viable observing site for EIGSEP and for development and testing of the instrument. This section gives an overview of the site and the deployments to date.

5.1 Site Selection

A suitable site to deploy EIGSEP needs to have low levels of RFI and feature a canyon large enough to provide a 100 m air gap for the suspended antenna. It is also advantageous that the site is easily accessible from Berkeley, California, while the instrument is still under active development at the University of California Berkeley. The search for a site was therefore restricted to the western United States. To find candidate sites, we combined maps of radio transmitters from the Federal Communications Commission⁶ with digital elevation maps from the US Geological Survey⁷. The combined map is presented in Fig. 12. Using this map, the site was selected from the areas outside the 60 dBu contours of the registered transmitters that also featured canyons more than 100 m deep.

With a dozen candidate sites selected, we conducted RFI surveys and a terrain inspection in 2022. The RFI level was measured with a discone antenna and a Keysight FieldFox Handheld RF analyzer⁸. From these field measurements, Marjum Pass was selected

⁶ <https://www.fcc.gov/media/radio/fm-query> for FM radio transmitters and <https://www.fcc.gov/media/television/tv-query> for digital TV transmitters.

⁷ <https://www.usgs.gov/3d-elevation-program>

⁸ <https://www.keysight.com/us/en/products/network-analyzers/fieldfox-handheld-rf-microwave-analyzers.html>

as a promising candidate site. It also featured several possible suspension points for the antenna. Additional measurements at Marjum Pass in 2023, with a prototype of the EIGSEP instrument, confirmed that the site provides a good compromise between RFI, terrain, and accessibility for EIGSEP.

5.2 RFI

Field measurements at Marjum Pass reveal reflected FM radio as the main source of RFI, primarily reflected off airplanes and, to a lesser extent, off meteor trails. Fig. 13 shows cross-correlation measurements from the two ground antennas at the site as a function of time and frequency. RFI is generally always present in five frequency channels in the FM band (88–108 MHz).

When an airplane is above the antenna, it reflects RFI from nearby transmitters, causing interference across the FM radio band. The signature of this airplane-reflected RFI is seen for example right before 13:30 in Fig. 13, where the power increases for about two minutes in the FM band. A similar effect, but at shorter time-scales – generally less than five seconds – is seen, for example at 14:00. We believe this is FM transmission reflected from meteor trails of electrons in the ionosphere; an effect that has been observed for decades (e.g. Hey et al. 1947; Ellyett & Davies 1948) and more recently in Helmboldt et al. (2014).

Because of low-duty-cycle RFI on site associated with aircraft transmission, we used flight data from flightradar24.com in combination with our horizon model (Fig. 11) to model airplane visibility above the horizon seen from the antenna. The results, displayed in Fig. 14, suggest that nighttime is relatively flight-free, yielding conservatively ≈ 7 hours of observing per night with no aircraft above the horizon.

In addition to RFI associated with FM radio, we see RFI from digital TV transmission at a lower level. This is not apparent in Fig. 13, but is seen in longer integrations at frequencies below FM.

5.3 Terrain and Geology of Site

The Dome Canyon runs north-south through the House Range mountains of west-central Utah (Millard County) between Howell Peak to the north and Sawtooth mountain to the south. At the site of the antenna, the eastern rim of the canyon is about 200 m above the canyon floor, while the western rim is about 380 m high. The bedrock consists predominantly of cliff-forming limestone with interbedded slope-forming shale (Hintze 1974). The sedimentary units in this sequence dip gently ($\approx 15^\circ$) toward the southeast at the location of the canyon, but dip orientation and magnitude varies regionally due to deformation and rotation of bedrock blocks associated with very steeply-dipping normal faults which generally trend north-south.

We were unable to find any published studies of ground penetrating radar surveys at our site that might provide direct measurements of the dielectric properties of these specific limestone and shale units. However, published values for the dielectric constant and conductivity of limestone generally lie within 7–9.2 (Parasnis 1956) and $0.003\text{--}0.3 \text{ mS m}^{-1}$ (Fechner et al. 2004), respectively, at a frequency range of 0.3–1000 MHz. The range of values presented for these properties depend on limestone composition, presence of impurities, and water content (Fechner et al. 2004). For example, the conductivity of dry, pure limestone is 0.003 mS m^{-1} but increases to $\approx 5 \text{ mS m}^{-1}$ for pure limestone with pore space saturation of 50 per cent (fig. 4 in Fechner et al. 2004). In the same figure, Fechner et al. (2004) show that the dielectric constant increases from ≈ 4 for dry limestone to ≈ 17 for pore space saturation of 50 per cent.

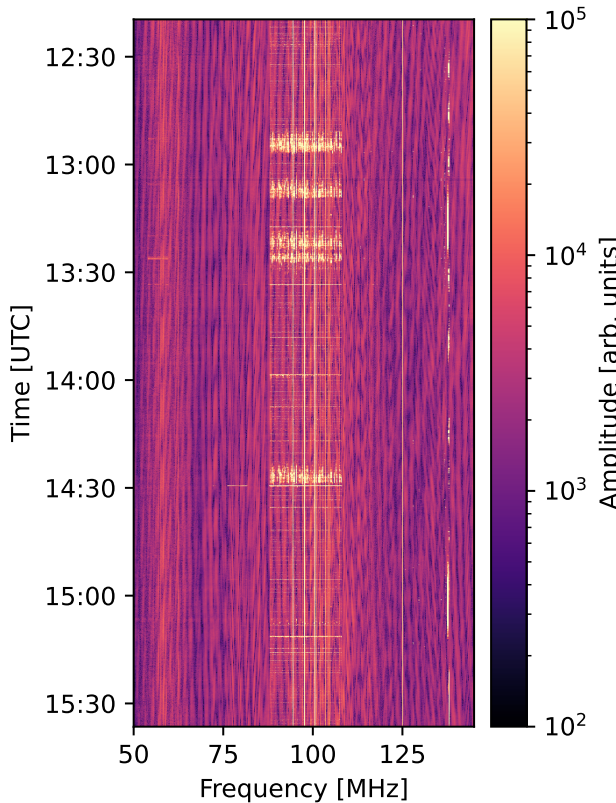


Figure 13. The measurements represent raw cross-correlation data from the correlator in logarithmic units taken on 2024 July 21. The integration time of each spectrum is 1.07 s. When the sky is free of reflectors, the spectra show low levels of RFI, even in the FM band. With airplanes or micrometeors overhead, significant RFI is present. Longer periods of RFI in the FM band (e.g. the feature right before 13:30) are associated with aircraft, whereas short blips (e.g. at 14:00) are associated with micrometeors. The transmission at 137 MHz is from Orbcomm satellites.

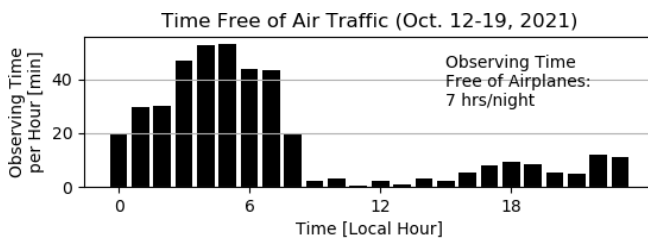


Figure 14. Observing time free of airplane traffic, computed from a horizon model and weekly flight information from flightradar24.com. This site conservatively yields seven hours of airplane-free observing per night.

The dielectric properties of shale exhibit similar variability to those of limestone, which are largely attributed, again, to water content. At 100 MHz, the dielectric constant of dry shale is about 5, compared to a value of 8 for water-saturated shale. Furthermore, there is a frequency dependence to the shale conductivity measured by [Josh et al. \(2016\)](#) with a 50 MHz signal giving a value of 10 mS m^{-1} which increases to roughly 13 mS m^{-1} at 100 MHz.

The complex spatial and spectral dependence of the electrical conductivity and permittivity of the soil again illustrate the importance

of separating the antenna from the ground for EIGSEP. While there are observing sites where the soil can be modelled well with simpler models ([Sutinjo et al. 2015](#); [Mahesh et al. 2021](#); [Spinelli et al. 2022](#); [Hendrickson et al. 2026](#)), they may still produce spectral artifacts in the antenna beam that must be well understood and calibrated.

5.4 Suspensions

The antenna is suspended using a highline between the eastern and western canyon rims. The highline is anchored to trees on each side. The choice of anchoring points defines the position of the elevated antenna. Using digital elevation maps of the site, the anchor points were decided based on accessibility and the horizon profile seen by the antenna. The horizon profile changes substantially between anchor points. As the canyon walls provide significant shielding from RFI, and the dominant source of RFI is reflections off airplanes, it is preferable for EIGSEP to have as small field of view to the sky as possible despite the cost of a higher fraction of ground radiation in the total antenna temperature.

Another critical consideration is the tension in the ropes. The vertical component of the tension force needs to balance the gravitational force on the antenna platform. If the antenna is raised too high relative to the top of the canyon walls, the total tension will increase sharply. This increase is seen intuitively in the hypothetical extreme where the antenna approaches the top of the canyon walls; in this scenario, the vertical component of the tension would go to zero and the required total tension would go to infinity to compensate. Anchor points at a much greater height than the target suspension height must therefore be used.

The final anchor points were chosen based on the horizon profiles, tension requirements, and accessibility. The highline is set up and anchored by a team of professional climbers from Sea to Sky Explorer's Association⁹. After initial set-up, the antenna is raised from the ground using the pulley system. This system gives flexibility to change batteries or make necessary fixes to the instrument without climbing to the top of the canyon. It also allows for changing the height during observation to assess the effect of a changing horizon profile or evaluate terrain coupling.

5.5 Field Measurements

Three versions of the EIGSEP instrument have been suspended. In July 2024, a prototype platform was suspended about 20 m above the ground at a nearby site. This test resulted in the first measurements taken by EIGSEP from above the ground, and demonstrated the use of a rotating antenna. The suspension with the highline and pulley system was first used at the current site in October 2024, using a Vivaldi feed of the same kind as the ground antennas. This feed was suspended about 95 m above the ground.

The new bowtie antenna and antenna platform were suspended in July 2025 for four days. During this period, the antenna was lowered and raised several times. The antenna was rotated continuously for approximately five hours each day, and the external calibration signal was continuously transmitted from the short dipole antenna. Additionally, reflection coefficient measurements and calibration measurements were taken for the first time for EIGSEP.

Analysis of data taken in the field, particularly from the deployments in October 2024 and July 2025, is in progress. Early results

⁹ <https://www.stsea.org/>

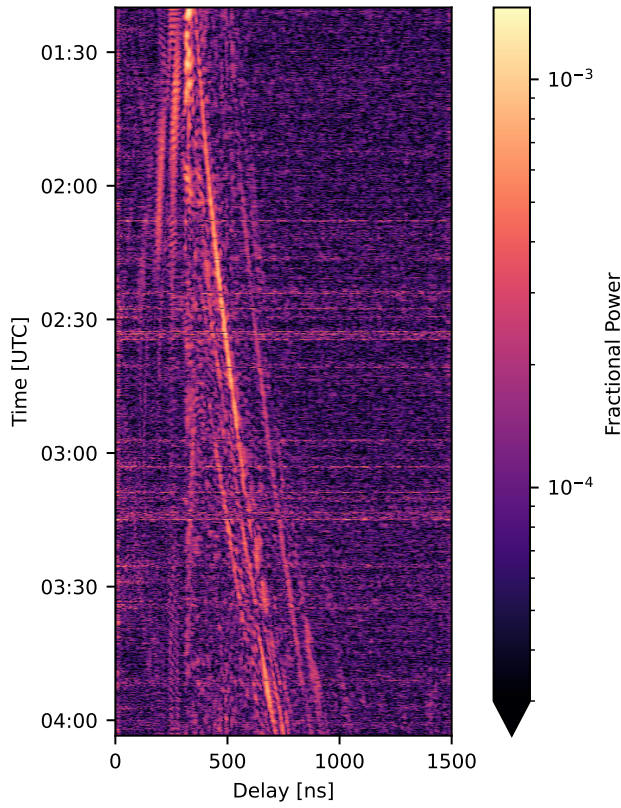


Figure 15. Delay spectrum of DPSS-filtered autocorrelation data from a ground-based Vivaldi feed. The data were taken on 2024 Oct 19. The spectrum is normalized by the total power received at each time. The diagonal lines reveal emission from Virgo A, scattering off distinct features in the terrain. Note the logarithmic colour scale, clipped at 3×10^{-5} to suppress noise.

from the October 2024 dataset reveal evidence of multipath scattering from Virgo A, detected in delay-transformed autocorrelation data from one of the ground-based Vivaldi feeds. To isolate the point source, we flag RFI in the raw autocorrelation data and use a filter based on discrete prolate spheroidal sequences (DPSS; Slepian 1978) to remove spectrally smooth foregrounds. As noted by Ewall-Wice et al. (2021), these sequences are optimal for suppressing power within a finite band in Fourier space. Fig. 15 displays the delay spectrum of the residuals after DPSS-filtering the data, normalised by the total power measured at each time. Diagonal tracks appear in these residuals, corresponding to the time-varying geometric delay of Virgo A as it transits. The multiple tracks appear due to reflections from different parts of the canyon. We attribute these tracks to Virgo A as it is the only bright point source above the canyon walls throughout the observation. These results are consistent with the known position of Virgo A during the observation, assuming that the dominant scatterer is the eastern canyon wall.

5.6 Ongoing and Future Work

Following the deployment in 2025, work is in progress to identify and characterise instrumental systematics in the data. Specifically, tests are conducted to evaluate the temporal stability of the instrument and how sensitive the instrument is to thermal variations. These tests will inform the strategy for the receiver calibration in the field. Work

is also done in the laboratory to identify self-induced RFI, which represents the dominant systematic in field measurements. Necessary upgrades to the instrument will be made to mitigate self-RFI and instrumental systematics. In addition, we are implementing the absolute receiver calibration described in Section 4.2 and analysing the beam mapping data described in 4.5.

In 2026, the improved instrument will again be deployed in the field for longer observations, with a focus on obtaining absolutely calibrated sky spectra, independent beam-weightings of the sky from different orientations of the antenna, and measurements of the antenna beam that can be compared to and validate simulations.

6 CONCLUSIONS

We have presented the EIGSEP experiment to measure the global 21-cm signal from Cosmic Dawn. EIGSEP uses one suspended antenna and two ground antennas, observing over 50–250 MHz. The key design consideration for EIGSEP is minimising instrumental systematics with spectral structure that, when coupled to bright foregrounds, may mimic the cosmological signal. To minimise the problematic systematics, EIGSEP employs a rotating bowtie antenna suspended in a canyon, with an ~ 100 m air bubble surrounding the antenna. We presented the bowtie antenna design and our approach for characterizing the antenna beam with a ground-based transmitter. We then presented our plans for calibration of the instrument, including field measurements of internal calibrators, external signal injection, reflection coefficient measurements, interferometric measurements, and lab characterisation.

The EIGSEP experiment has been deployed at Marjum Pass four times, most recently in July 2025 with the custom bowtie antenna on a rotating antenna platform. The site exhibits a clean radio frequency environment, with transient reflections of transmitters off airplanes representing the primary source interference. Initial data analysis show terrain scattering of emission from Virgo A.

Future work is focused on data analysis, laboratory characterization of the receiver and mitigation of self-interference. The results of these efforts will be used to identify and remove instrumental systematics. In parallel, analysis of transmitter data is underway to attempt to characterise the antenna beam and validate numerical simulations. With the better characterised instrument, we plan on making extended sky measurements in 2026.

ACKNOWLEDGEMENTS

We thank Khaled Allen, Sam Cipriani, Chris Gill, Yongsheng Li, Sam Ludwig, Ashlie Reott, Elon Smith, Grant Syllaba, and Sean Taylor from Sea to Sky Explorers Association for help with suspensions of the instrument. We thank Ken Parsons for help with site selection and contributions during deployments. We thank Judah, Elena, and Greta Spiegel for help with deployments. We thank Kiran Shila and the DSA-2000 collaboration for sharing the design of the RFoF board. This research is funded by the Gordon and Betty Moore Foundation, Grant GBMF12211.

DATA AVAILABILITY

Data, simulation results, and code used to generate the plots is publicly available on Zenodo at <https://doi.org/10.5281/zenodo.18383267>. The code is also available on GitHub at https://github.com/christianhbye/eigsep_paper_notebooks. The

design of the RFoF board is available on GitHub at <https://github.com/liuweiseu/rfov-ftx/tree/cefad78>.

REFERENCES

Abdurashidova, Z. et al., 2022. HERA Phase I Limits on the Cosmic 21 cm Signal: Constraints on Astrophysics and Cosmology during the Epoch of Reionization, *ApJ*, **924**(2), 51.

Agrawal, Y., Kavitha, K., & Singh, S., 2024. Direction-dependent Effects on Global 21 cm Detection, *ApJ*, **974**(1), 137.

Altamirano, C. et al., 2025. Using the Antenna Impedance to Estimate Soil Electrical Parameters for the MIST Global 21 cm Experiment, *PASP*, **137**(8), 085002.

Anstey, D., de Lera Acedo, E., & Handley, W., 2021. A general Bayesian framework for foreground modelling and chromaticity correction for global 21 cm experiments, *MNRAS*, **506**(2), 2041–2058.

Anstey, D., de Lera Acedo, E., & Handley, W., 2023. Use of time dependent data in Bayesian global 21-cm foreground and signal modelling, *MNRAS*, **520**(1), 850–865.

Artuc, K. & de Lera Acedo, E., 2025. The spectrometer development of CosmoCube, lunar orbiting satellite to detect 21-cm hydrogen signal from cosmic dark ages, *RAS Techniques and Instruments*, **4**, rzae061.

Baars, J. W. M., Genzel, R., Pauliny-Toth, I. I. K., & Witzel, A., 1977. The absolute spectrum of Cas A: an accurate flux density scale and a set of secondary calibrators., *A&A*, **61**, 99–106.

Balanis, C. A., 1982. *Antenna Theory: Analysis and Design*, John Wiley & Sons, New York, 1st edn.

Bale, S. D. et al., 2023. LuSEE 'Night': The Lunar Surface Electromagnetics Experiment, *arXiv e-prints*, p. arXiv:2301.10345.

Barkana, R., 2016. The rise of the first stars: Supersonic streaming, radiative feedback, and 21-cm cosmology, *Phys. Rep.*, **645**, 1–59.

Barkana, R., 2018. Possible interaction between baryons and dark-matter particles revealed by the first stars, *Nature*, **555**(7694), 71–74.

Bassett, N., Rapetti, D., Tauscher, K., Nhan, B. D., Bordenave, D. D., Hibbard, J. J., & Burns, J. O., 2021. Lost Horizon: Quantifying the Effect of Local Topography on Global 21 cm Cosmology Data Analysis, *ApJ*, **923**(1), 33.

Becker, G. D., Bolton, J. S., Madau, P., Pettini, M., Ryan-Weber, E. V., & Venemans, B. P., 2015. Evidence of patchy hydrogen reionization from an extreme Ly α trough below redshift six, *MNRAS*, **447**(4), 3402–3419.

Berkhout, L. M. et al., 2024. Hydrogen Epoch of Reionization Array (HERA) Phase II Deployment and Commissioning, *PASP*, **136**(4), 045002.

Bernardi, G., McQuinn, M., & Greenhill, L. J., 2015. Foreground Model and Antenna Calibration Errors in the Measurement of the Sky-averaged λ 21 cm Signal at $z \sim 20$, *ApJ*, **799**(1), 90.

Bevis, H. T. J., Handley, W. J., Fialkov, A., de Lera Acedo, E., Greenhill, L. J., & Price, D. C., 2021. MAXSMOOTH: rapid maximally smooth function fitting with applications in Global 21-cm cosmology, *MNRAS*, **502**(3), 4405–4425.

Bosman, S. E. I., Fan, X., Jiang, L., Reed, S., Matsuoka, Y., Becker, G., & Haehnelt, M., 2018. New constraints on Lyman- α opacity with a sample of 62 quasars at $z > 5.7$, *MNRAS*, **479**(1), 1055–1076.

Bosman, S. E. I. et al., 2022. Hydrogen reionization ends by $z = 5.3$: Lyman- α optical depth measured by the XQR-30 sample, *MNRAS*, **514**(1), 55–76.

Bowman, J. D., Rogers, A. E. E., Monsalve, R. A., Mozdzen, T. J., & Mahesh, N., 2018. An absorption profile centred at 78 megahertz in the sky-averaged spectrum, *Nature*, **555**(7694), 67–70.

Bradley, R. F., Tauscher, K., Rapetti, D., & Burns, J. O., 2019. A Ground Plane Artifact that Induces an Absorption Profile in Averaged Spectra from Global 21 cm Measurements, with Possible Application to EDGES, *ApJ*, **874**(2), 153.

Bull, P. et al., 2025. RHINO: a large horn antenna for detecting the 21 cm global signal, *RAS Techniques and Instruments*, **4**, rzaf046.

Cappallo, R. C. et al., 2025. EDGES-3: Instrument Design and Commissioning, *PASP*, **137**(12), 125002.

Castellano, M. et al., 2022. Early Results from GLASS-JWST. III. Galaxy Candidates at $z \sim 9$ –15, *ApJ*, **938**(2), L15.

Chen, X., Yan, J., Deng, L., Wu, F., Wu, L., Xu, Y., & Zhou, L., 2021. Discovering the sky at the longest wavelengths with a lunar orbit array, *Philosophical Transactions of the Royal Society of London Series A*, **379**(2188), 20190566.

Cumner, J. et al., 2022. Radio Antenna Design for Sky-Averaged 21cm Cosmology Experiments: The REACH Case, *Journal of Astronomical Instrumentation*, **11**(1), 2250001–2058.

Cumner, J., Pieterse, C., de Villiers, D., & de Lera Acedo, E., 2024. The effects of the antenna power pattern uncertainty within a global 21 cm experiment, *MNRAS*, **531**(4), 4734–4745.

Datta, A., Bradley, R., Burns, J. O., Harker, G., Komjathy, A., & Lazio, T. J. W., 2016. The Effects of the Ionosphere on Ground-based Detection of the Global 21 cm Signal from the Cosmic Dawn and the Dark Ages, *ApJ*, **831**(1), 6.

de Lera Acedo, E. et al., 2022. The REACH radiometer for detecting the 21-cm hydrogen signal from redshift $z \approx 7.5$ –28, *Nature Astronomy*, **6**, 984–998.

de Oliveira-Costa, A., Tegmark, M., Gaensler, B. M., Jonas, J., Landecker, T. L., & Reich, P., 2008. A model of diffuse Galactic radio emission from 10 MHz to 100 GHz, *MNRAS*, **388**(1), 247–260.

DeBoer, D. R. et al., 2017. Hydrogen Epoch of Reionization Array (HERA), *PASP*, **129**(974), 045001.

Dewdney, P. E., Hall, P. J., Schilizzi, R. T., & Lazio, T. J. L. W., 2009. The Square Kilometre Array, *IEEE Proceedings*, **97**(8), 1482–1496.

Di Matteo, T., Perna, R., Abel, T., & Rees, M. J., 2002. Radio Foregrounds for the 21 Centimeter Tomography of the Neutral Intergalactic Medium at High Redshifts, *ApJ*, **564**(2), 576–580.

Eastwood, M. W. et al., 2019. The 21 cm Power Spectrum from the Cosmic Dawn: First Results from the OVRO-LWA, *AJ*, **158**(2), 84.

Eilers, A.-C., Davies, F. B., & Hennawi, J. F., 2018. The Opacity of the Intergalactic Medium Measured along Quasar Sightlines at $z \sim 6$, *ApJ*, **864**(1), 53.

Ellyett, C. D. & Davies, J. G., 1948. Velocity of Meteors Measured by Diffraction of Radio Waves from Trails during Formation, *Nature*, **161**(4094), 596–597.

Ewall-Wice, A. et al., 2016. First limits on the 21 cm power spectrum during the Epoch of X-ray heating, *MNRAS*, **460**(4), 4320–4347.

Ewall-Wice, A., Chang, T.-C., Lazio, J., Doré, O., Seiffert, M., & Monsalve, R. A., 2018. Modeling the Radio Background from the First Black Holes at Cosmic Dawn: Implications for the 21 cm Absorption Amplitude, *ApJ*, **868**(1), 63.

Ewall-Wice, A., Chang, T.-C., & Lazio, T. J. W., 2020. The Radio Scream from black holes at Cosmic Dawn: a semi-analytic model for the impact of radio-loud black holes on the 21 cm global signal, *MNRAS*, **492**(4), 6086–6104.

Ewall-Wice, A. et al., 2021. DAYENU: a simple filter of smooth foregrounds for intensity mapping power spectra, *MNRAS*, **500**(4), 5195–5213.

Fagnoni, N., de Lera Acedo, E., Drought, N., DeBoer, D. R., Riley, D., Razavi-Ghods, N., Carey, S., & Parsons, A. R., 2021. Design of the New Wideband Vivaldi Feed for the HERA Radio-Telescope Phase II, *IEEE Transactions on Antennas and Propagation*, **69**(12), 8143–8157.

Fan, X. et al., 2006. Constraining the Evolution of the Ionizing Background and the Epoch of Reionization with $z \sim 6$ Quasars. II. A Sample of 19 Quasars, *AJ*, **132**(1), 117–136.

Fechner, T., Börner, F. D., Richter, T., Yaramanci, U., & Weihnacht, B., 2004. Lithological interpretation of the spectral dielectric properties of limestone, *Near Surface Geophysics*, **2**(3), 151–159.

Feng, C. & Holder, G., 2018. Enhanced Global Signal of Neutral Hydrogen Due to Excess Radiation at Cosmic Dawn, *ApJ*, **858**(2), L17.

Fialkov, A. & Loeb, A., 2016. Precise Measurement of the Reionization Optical Depth from the Global 21 cm Signal Accounting for Cosmic Heating, *ApJ*, **821**(1), 59.

Finkelstein, S. L. et al., 2023. CEERS Key Paper. I. An Early Look into the First 500 Myr of Galaxy Formation with JWST, *ApJ*, **946**(1), L13.

Fraser, S. et al., 2018. The EDGES 21 cm anomaly and properties of dark matter, *Physics Letters B*, **785**, 159–164.

Furlanetto, S. R., Oh, S. P., & Briggs, F. H., 2006. Cosmology at low frequencies: The 21 cm transition and the high-redshift Universe, *Phys. Rep.*,

433(4-6), 181–301.

Ghara, R. et al., 2020. Constraining the intergalactic medium at $z \approx 9.1$ using LOFAR Epoch of Reionization observations, *MNRAS*, **493**(4), 4728–4747.

Ghara, R. et al., 2025. Constraints on the state of the intergalactic medium at $z \sim 8 - 10$ using redshifted 21 cm observations with LOFAR, *A&A*, **699**, A109.

Greig, B. et al., 2021. Interpreting LOFAR 21-cm signal upper limits at $z \approx 9.1$ in the context of high- z galaxy and reionization observations, *MNRAS*, **501**(1), 1–13.

Hallinan, G. et al., 2019. The DSA-2000 — A Radio Survey Camera, in *Bulletin of the American Astronomical Society*, vol. 51, p. 255.

van Harleem, M. P. et al., 2013. LOFAR: The LOw-Frequency ARray, *A&A*, **556**, A2.

Helmboldt, J. F., Ellingson, S. W., Hartman, J. M., Lazio, T. J. W., Taylor, G. B., Wilson, T. L., & Wolfe, C. N., 2014. All-sky imaging of meteor trails at 55.25 MHz with the first station of the Long Wavelength Array, *Radio Science*, **49**(3), 157–180.

Hendrickson, I. et al., 2026. Estimating soil electrical parameters in the Canadian High Arctic from impedance measurements of the MIST antenna above the surface, *Geophysical Research Letters*, **53**(2), e2025GL116618, e2025GL116618 2025GL116618.

HERA Collaboration et al., 2023. Improved Constraints on the 21 cm EoR Power Spectrum and the X-Ray Heating of the IGM with HERA Phase I Observations, *ApJ*, **945**(2), 124.

Hey, J. S., Parsons, S. J., & Stewart, G. S., 1947. Radar observations of the Giacobinids meteor shower, 1946, *MNRAS*, **107**, 176.

Hickish, J. et al., 2016. A Decade of Developing Radio-Astronomy Instrumentation using CASPER Open-Source Technology, *Journal of Astronomical Instrumentation*, **5**(4), 1641001–12.

Hills, R., Kulkarni, G., Meerburg, P. D., & Puchwein, E., 2018. Concerns about modelling of the EDGES data, *Nature*, **564**(7736), E32–E34.

Hintze, L. F., 1974. Preliminary geologic map of the Notch Peak quadrangle, Millard County, Utah, U.S. Geological Survey, Map.

Jishnu Nambissan, T. et al., 2021. SARAS 3 CD/EoR radiometer: design and performance of the receiver, *Experimental Astronomy*, **51**(2), 193–234.

Josh, M., Clennell, B., & Cauchefert, M., 2016. Dielectric permittivity and anisotropy of intact multi-saturated organic shales, in *SPWLA 57th Annual Logging Symposium*, Reykjavik, Iceland, Paper presented at the SPWLA 57th Annual Logging Symposium.

Kern, N. S., Parsons, A. R., Dillon, J. S., Lanman, A. E., Fagnoni, N., & de Lera Acedo, E., 2019. Mitigating Internal Instrument Coupling for 21 cm Cosmology. I. Temporal and Spectral Modeling in Simulations, *ApJ*, **884**(2), 105.

Kulkarni, G., Keating, L. C., Haehnelt, M. G., Bosman, S. E. I., Puchwein, E., Chardin, J., & Aubert, D., 2019. Large Ly α opacity fluctuations and low CMB τ in models of late reionization with large islands of neutral hydrogen extending to $z < 5.5$, *MNRAS*, **485**(1), L24–L28.

Liu, A. & Parsons, A. R., 2016. Constraining cosmology and ionization history with combined 21 cm power spectrum and global signal measurements, *MNRAS*, **457**(2), 1864–1877.

Liu, A. & Shaw, J. R., 2020. Data Analysis for Precision 21 cm Cosmology, *PASP*, **132**(1012), 062001.

Liu, A., Pritchard, J. R., Tegmark, M., & Loeb, A., 2013. Global 21 cm signal experiments: A designer's guide, *Phys. Rev. D*, **87**(4), 043002.

Liu, A., Pritchard, J. R., Allison, R., Parsons, A. R., Seljak, U., & Sherwin, B. D., 2016a. Eliminating the optical depth nuisance from the CMB with 21 cm cosmology, *Phys. Rev. D*, **93**(4), 043013.

Liu, C., Mutch, S. J., Angel, P. W., Duffy, A. R., Geil, P. M., Poole, G. B., Mesinger, A., & Wyithe, J. S. B., 2016b. Dark-ages reionization and galaxy formation simulation - IV. UV luminosity functions of high-redshift galaxies, *MNRAS*, **462**(1), 235–249.

Madau, P., Meiksin, A., & Rees, M. J., 1997. 21 Centimeter Tomography of the Intergalactic Medium at High Redshift, *ApJ*, **475**(2), 429–444.

Mahesh, N., Bowman, J. D., Mozdzen, T. J., Rogers, A. E. E., Monsalve, R. A., Murray, S. G., & Lewis, D., 2021. Validation of the EDGES Low-band Antenna Beam Model, *AJ*, **162**(2), 38.

Mason, C. A., Trenti, M., & Treu, T., 2015. The Galaxy UV Luminosity Function before the Epoch of Reionization, *ApJ*, **813**(1), 21.

McKay, L., Subrahmanyam, R., Chippendale, A., Bolli, P., Kyriakou, G., Dunning, A., & Ekers, R., 2025. Precise Measurement of the Absolute Sky Brightness at 60 to 350 MHz, *arXiv e-prints*, p. arXiv:2509.11846.

McLeod, D. J., McLure, R. J., Dunlop, J. S., Robertson, B. E., Ellis, R. S., & Targett, T. A., 2015. New redshift $z \approx 9$ galaxies in the Hubble Frontier Fields: implications for early evolution of the UV luminosity density, *MNRAS*, **450**(3), 3032–3044.

McQuinn, M., Hernquist, L., Zaldarriaga, M., & Dutta, S., 2007. Studying reionization with Ly α emitters, *MNRAS*, **381**(1), 75–96.

Meyer, R. A., Roberts-Borsani, G., Oesch, P. A., & Ellis, R. S., 2025. Probing patchy reionization with JWST: IGM opacity constraints from the Lyman α forest of galaxies in legacy extragalactic fields, *MNRAS*, **542**(3), 1952–1968.

Meys, R. P., 1978. A Wave Approach to the Noise Properties of Linear Microwave Devices, *IEEE Transactions on Microwave Theory and Techniques*, **26**(1), 34–37.

Mirocha, J. & Furlanetto, S. R., 2019. What does the first highly redshifted 21-cm detection tell us about early galaxies?, *MNRAS*, **483**(2), 1980–1992.

Mirocha, J., Furlanetto, S. R., & Sun, G., 2017. The global 21-cm signal in the context of the high- z galaxy luminosity function, *MNRAS*, **464**(2), 1365–1379.

Mondal, R. et al., 2020. Tight constraints on the excess radio background at $z = 9.1$ from LOFAR, *MNRAS*, **498**(3), 4178–4191.

Monsalve, R. A., Rogers, A. E. E., Bowman, J. D., & Mozdzen, T. J., 2017a. Calibration of the EDGES High-band Receiver to Observe the Global 21 cm Signature from the Epoch of Reionization, *ApJ*, **835**(1), 49.

Monsalve, R. A., Rogers, A. E. E., Bowman, J. D., & Mozdzen, T. J., 2017b. Results from EDGES High-band. I. Constraints on Phenomenological Models for the Global 21 cm Signal, *ApJ*, **847**(1), 64.

Monsalve, R. A. et al., 2024a. Mapper of the IGM spin temperature: instrument overview, *MNRAS*, **530**(4), 4125–4147.

Monsalve, R. A. et al., 2024b. Simulating the Detection of the Global 21 cm Signal with MIST for Different Models of the Soil and Beam Directivity, *ApJ*, **961**(1), 56.

Mozdzen, T. J., Bowman, J. D., Monsalve, R. A., & Rogers, A. E. E., 2016. Limits on foreground subtraction from chromatic beam effects in global redshifted 21 cm measurements, *MNRAS*, **455**(4), 3890–3900.

Muñoz, J. B. & Loeb, A., 2018. A small amount of mini-charged dark matter could cool the baryons in the early Universe, *Nature*, **557**(7707), 684–686.

Munshi, S. et al., 2024. First upper limits on the 21 cm signal power spectrum from cosmic dawn from one night of observations with NenuFAR, *A&A*, **681**, A62.

Naidu, R. P. et al., 2022. Two Remarkably Luminous Galaxy Candidates at $z \approx 10-12$ Revealed by JWST, *ApJ*, **940**(1), L14.

Oh, S. P. & Mack, K. J., 2003. Foregrounds for 21-cm observations of neutral gas at high redshift, *MNRAS*, **346**(3), 871–877.

Ota, K. et al., 2017. A New Constraint on Reionization from the Evolution of the Ly α Luminosity Function at $z \sim 6-7$ Probed by a Deep Census of $z = 7.0$ Ly α Emitter Candidates to $0.3L^*$, *ApJ*, **844**(1), 85.

Parasnis, D. S., 1956. The electrical resistivity of some sulphide and oxide minerals and their ores, *Geophysical Prospecting*, **4**(3), 249–278.

Parsons, A. R. et al., 2010. The Precision Array for Probing the Epoch of Re-ionization: Eight Station Results, *AJ*, **139**(4), 1468–1480.

Pattison, J. H. N., Anstey, D. J., & de Lera Acedo, E., 2024. Modelling a hot horizon in global 21-cm experimental foregrounds, *MNRAS*, **527**(2), 2413–2425.

Perley, R. A. & Butler, B. J., 2017. An Accurate Flux Density Scale from 50 MHz to 50 GHz, *ApJS*, **230**(1), 7.

Philip, L. et al., 2019. Probing Radio Intensity at High-Z from Marion: 2017 Instrument, *Journal of Astronomical Instrumentation*, **8**(2), 1950004.

Planck Collaboration et al., 2020. Planck 2018 results. VI. Cosmological parameters, *A&A*, **641**, A6.

Pospelov, M., Pradler, J., Ruderman, J. T., & Urbano, A., 2018. Room for New Physics in the Rayleigh-Jeans Tail of the Cosmic Microwave Background, *Phys. Rev. Lett.*, **121**(3), 031103.

Price, D. C. et al., 2018. Design and characterization of the Large-aperture Experiment to Detect the Dark Age (LEDA) radiometer systems, *MNRAS*, **478**(3), 4193–4213.

Pritchard, J. R. & Loeb, A., 2010. Constraining the unexplored period between the dark ages and reionization with observations of the global 21 cm signal, *Phys. Rev. D*, **82**(2), 023006.

Raghunathan, A. et al., 2021. A Floating Octave Bandwidth Cone-Disk Antenna for Detection of Cosmic Dawn, *IEEE Transactions on Antennas and Propagation*, **69**(10), 6209–6217.

Reichardt, C. L. et al., 2021. An Improved Measurement of the Secondary Cosmic Microwave Background Anisotropies from the SPT-SZ + SPTpol Surveys, *ApJ*, **908**(2), 199.

Rogers, A. E. E. & Bowman, J. D., 2012. Absolute calibration of a wideband antenna and spectrometer for accurate sky noise temperature measurements, *Radio Science*, **47**(4), RS0K06.

Sathyaranayana Rao, M., Subrahmanyam, R., Udaya Shankar, N., & Chluba, J., 2017a. GM OSS: All-sky Model of Spectral Radio Brightness Based on Physical Components and Associated Radiative Processes, *AJ*, **153**(1), 26.

Sathyaranayana Rao, M., Subrahmanyam, R., Udaya Shankar, N., & Chluba, J., 2017b. Modeling the Radio Foreground for Detection of CMB Spectral Distortions from the Cosmic Dawn and the Epoch of Reionization, *ApJ*, **840**(1), 33.

Sathyaranayana Rao, M. et al., 2023. PRATUSH experiment concept and design overview, *Experimental Astronomy*, **56**(2–3), 741–778.

Saxena, A., Meerburg, P. D., de Lera Acedo, E., Handley, W., & Koopmans, L. V. E., 2023. Sky-averaged 21-cm signal extraction using multiple antennas with an SVD framework: the REACH case, *MNRAS*, **522**(1), 1022–1032.

Shaver, P. A., Windhorst, R. A., Madau, P., & de Bruyn, A. G., 1999. Can the reionization epoch be detected as a global signature in the cosmic background?, *A&A*, **345**, 380–390.

Shen, E., Anstey, D., de Lera Acedo, E., Fialkov, A., & Handley, W., 2021. Quantifying ionospheric effects on global 21-cm observations, *MNRAS*, **503**(1), 344–353.

Sikivie, P., 2019. Axion dark matter and the 21-cm signal, *Physics of the Dark Universe*, **24**, 100289.

Sims, P. H. & Pober, J. C., 2020. Testing for calibration systematics in the EDGES low-band data using Bayesian model selection, *MNRAS*, **492**(1), 22–38.

Singh, S. & Subrahmanyam, R., 2019. The Redshifted 21 cm Signal in the EDGES Low-band Spectrum, *ApJ*, **880**(1), 26.

Singh, S. et al., 2022. On the detection of a cosmic dawn signal in the radio background, *Nature Astronomy*, **6**, 607–617.

Slatyer, T. R. & Wu, C.-L., 2018. Early-Universe constraints on dark matter-baryon scattering and their implications for a global 21 cm signal, *Phys. Rev. D*, **98**(2), 023013.

Slepian, D., 1978. Prolate spheroidal wave functions, Fourier analysis, and uncertainty. V - The discrete case, *AT&T Technical Journal*, **57**, 1371–1430.

Spinelli, M., Kyriakou, G., Bernardi, G., Bolli, P., Greenhill, L. J., Fialkov, A., & Garsden, H., 2022. Antenna beam characterization for the global 21-cm experiment LEDA and its impact on signal model parameter reconstruction, *MNRAS*, **515**(2), 1580–1597.

Sutinjo, A. T. et al., 2015. Characterization of a Low-Frequency Radio Astronomy Prototype Array in Western Australia, *IEEE Transactions on Antennas and Propagation*, **63**(12), 5433–5442.

Switzer, E. R. & Liu, A., 2014. Erasing the Variable: Empirical Foreground Discovery for Global 21 cm Spectrum Experiments, *ApJ*, **793**(2), 102.

Tang, M., Stark, D. P., Topping, M. W., Mason, C., & Ellis, R. S., 2024. JWST/NIRSpec Observations of Lyman α Emission in Star-forming Galaxies at $6.5 \lesssim z \lesssim 13$, *ApJ*, **975**(2), 208.

Tauscher, K., Rapetti, D., & Burns, J. O., 2020. Global 21 cm Signal Extraction from Foreground and Instrumental Effects. III. Utilizing Drift-scan Time Dependence and Full Stokes Measurements, *ApJ*, **897**(2), 175.

Tingay, S. J. et al., 2013. The Murchison Widefield Array: The Square Kilometre Array Precursor at Low Radio Frequencies, *Publ. Astron. Soc. Australia*, **30**, e007.

Tozzi, P., Madau, P., Meiksin, A., & Rees, M. J., 2000. Radio Signatures of H I at High Redshift: Mapping the End of the “Dark Ages”, *ApJ*, **528**(2), 597–606.

Umeda, H. et al., 2025. SILVERRUSH. XIV. Ly α Luminosity Functions and Angular Correlation Functions from 20,000 Ly α Emitters at $z \sim 2.2$ –7.3 from up to 24 deg 2 HSC-SSP and CHORUS Surveys: Linking the Postreionization Epoch to the Heart of Reionization, *ApJS*, **277**(2), 37.

Vedantham, H. K., Koopmans, L. V. E., de Bruyn, A. G., Wijnholds, S. J., Ciardi, B., & Brentjens, M. A., 2014. Chromatic effects in the 21 cm global signal from the cosmic dawn, *MNRAS*, **437**(2), 1056–1069.

Wayth, R. B. et al., 2018. The Phase II Murchison Widefield Array: Design overview, *Publ. Astron. Soc. Australia*, **35**, e033.

Whitler, L. et al., 2025. The $z \gtrsim 9$ Galaxy UV Luminosity Function from the JWST Advanced Deep Extragalactic Survey: Insights into Early Galaxy Evolution and Reionization, *ApJ*, **992**(1), 63.

Witstok, J. et al., 2025. Witnessing the onset of reionization through Lyman- α emission at redshift 13, *Nature*, **639**(8056), 897–901.

Yang, Y., 2018. Contributions of dark matter annihilation to the global 21 cm spectrum observed by the EDGES experiment, *Phys. Rev. D*, **98**(10), 103503.

Zheng, H. et al., 2017. An improved model of diffuse galactic radio emission from 10 MHz to 5 THz, *MNRAS*, **464**(3), 3486–3497.

This paper has been typeset from a \TeX / \LaTeX file prepared by the author.